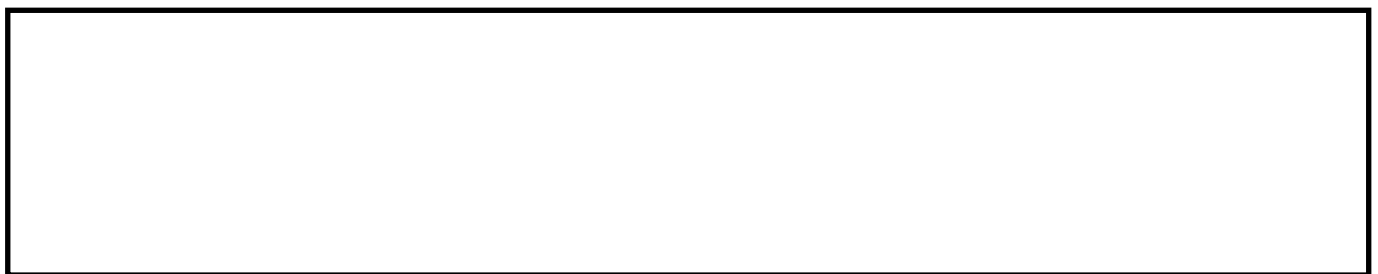


ZHAO, X., WANG, J., WANG, J., YANG, M., YAN, C., ZOU, G., TSE, J.S., FERNANDEZ, C. and PENG, Q. 2022. Atomically dispersed quintuple nitrogen and oxygen co-coordinated zirconium on graphene-type substrate for highly efficient oxygen reduction reaction. *Cell reports physical science* [online], 3(3), article 100773. Available from: <https://doi.org/10.1016/j.xcrp.2022.100773>

Atomically dispersed quintuple nitrogen and oxygen co-coordinated zirconium on graphene-type substrate for highly efficient oxygen reduction reaction.

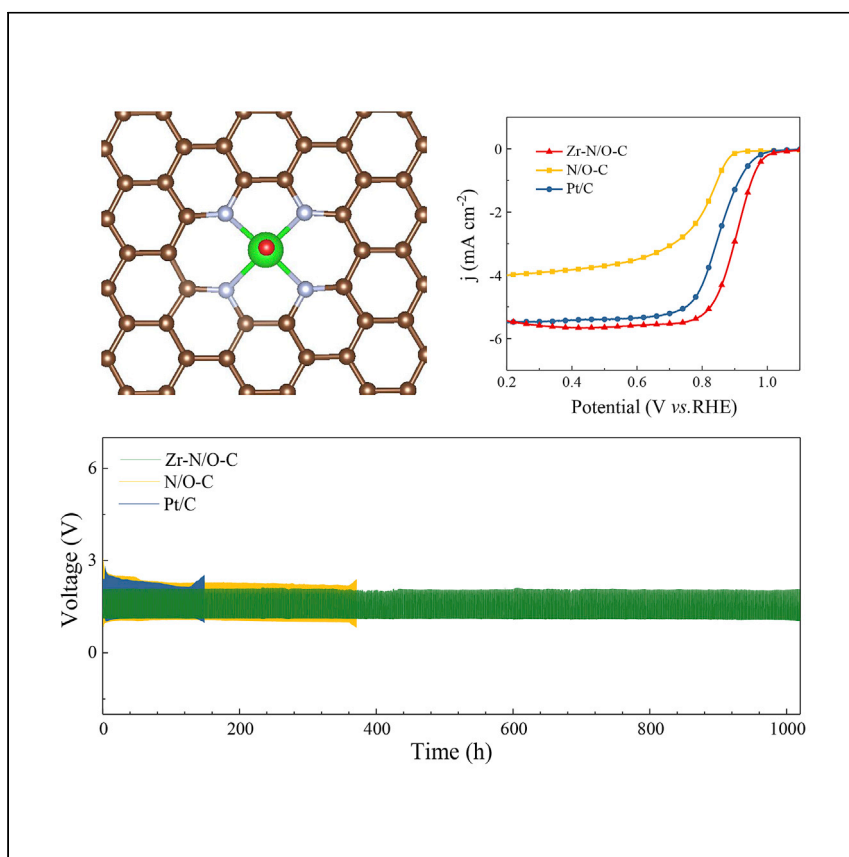
ZHAO, X., WANG, J., WANG, J., YANG, M., YAN, C., ZOU, G., TSE, J.S., FERNANDEZ, C. and PENG, Q.

2022



Article

Atomically dispersed quintuple nitrogen and oxygen co-coordinated zirconium on graphene-type substrate for highly efficient oxygen reduction reaction



Zhao et al. prepare a Zr-metal single atom catalyst by a ball-milling, solid-solution-assisted pyrolysis method. The catalyst exhibits notable ORR activity and long-life structural stability. It is demonstrated that the quintuple nitrogen and oxygen co-coordinated structure accounts for the high catalytic activity of the atomic Zr-metal core.

Xue Zhao, Jing Wang, Jinming Wang, ..., John S. Tse, Carlos Fernandez, Qiuming Peng

pengqiuming@ysu.edu.cn

Highlights

A large-scale method to prepare general M-N/O-C catalysts

The low-cost Zr-N/O-C catalyst exhibits a high half-wave potential of 0.910 V

Zn-air battery shows high cycling stability over a wide temperature range

Dual-ligand confinement accounts for high chemical activity of ZrN₄O moieties

Zhao et al., Cell Reports Physical Science 3, 100773

March 16, 2022 © 2022 The Authors.

<https://doi.org/10.1016/j.xcrp.2022.100773>



Article

Atomically dispersed quintuple nitrogen and oxygen co-coordinated zirconium on graphene-type substrate for highly efficient oxygen reduction reaction

Xue Zhao,^{1,5} Jing Wang,^{1,5} Jinming Wang,¹ Meng Yang,¹ Chenglin Yan,² Guodong Zou,¹ John S. Tse,³ Carlos Fernandez,⁴ and Qiuming Peng^{1,6,*}

SUMMARY

A cost-effective and long stability catalyst with decent electrochemical activity would play a crucial role in accelerating applications of metal-air batteries. Here, we report quintuple nitrogen and oxygen co-coordinated Zr sites on graphene (Zr-N/O-C) by using a ball-milling, solid-solution-assisted pyrolysis method. The as-prepared Zr-N/O-C catalyst with 2.93 wt % Zr shows a half-wave potential of 0.910 V, an onset potential of 1.000 V in 0.1 M KOH, impressive durability (95.1% remains after 16,000 s), and long-term stability (5 mV loss over 10,000 cycles). Zn-air batteries with the Zr-N/O-C electrode exhibit a maximum power density of 217.9 mW cm⁻² and a high cycling life of over 1,000 h, exceeding the counterpart equipped with a Pt/C benchmark. Theoretical simulations demonstrate that nitrogen and oxygen dual-ligand confinement effectively tunes the *d*-band center and balances key intermediates binding energy of intrinsic quintuple coordination Zr sites.

INTRODUCTION

Zn-air batteries are promising next-generation candidates with sustainable and safe merits in comparison to Li batteries.^{1–4} However, the shortage of suitable catalysis becomes a bottleneck in speeding up the pace in the use of Zn-air batteries.^{5,6} The commercial Pt-based catalyst has accounted for more than half of the total cell cost in carrying forward large-scale applications of clean energy devices and suffers from an unsustainable supply and increasing market price.^{4,7} The bio-inspired M-N-C (M = Fe, Co, Ni, Mn) catalysts composed of individual metals anchored by N on C substrates bring new opportunities. In these catalysts, MN_x moieties act as the active sites and can be developed as cost-effective and highly efficient alternatives.⁸ Nevertheless, studies have reported that catalysts do not meet the requirements for practical use, mainly due to the limited activity and unsatisfactory stability.⁹ It has been confirmed that the performance of these M-N-C compounds is intimately dependent on the metal elements. However, the available metal species cannot achieve high levels of activity together with long-term stability.^{10–14} For example, Fe-N-C was demonstrated to possess high oxygen reduction reaction (ORR) activity, yet it also tends to degrade quickly because the Fe²⁺ ion animates in side reactions.¹⁴ By contrast, Co-N-C improves the stability at the expense of selectivity, and the ORR activity of Mn-N-C or Ni-N-C is far behind that of Fe-N-C and Co-N-C.^{15–19} Therefore, fabricating operational MN_x motifs with competent elements is of significant importance but a great challenge.

¹State Key Laboratory of Metastable Materials Science and Technology, Yanshan University, Qinhuangdao 066004, P.R. China

²Suzhou Key Laboratory of Advanced Carbon Materials and Wearable Energy Technology, Soochow University, Suzhou 215006, P.R. China

³Department of Physics, University of Saskatchewan, Saskatoon, SK S7N5B2, Canada

⁴School of Pharmacy and Life Sciences, Robert Gordon University, AB107GJ Aberdeen, UK

⁵These authors contributed equally

⁶Lead contact

*Correspondence: pengqiuming@ysu.edu.cn
<https://doi.org/10.1016/j.xcrp.2022.100773>



The valence electron configuration of Zr is $4d^25s^2$, which bestows 5 completely empty *d* orbitals, theoretically for its cation (Zr^{4+}) and stronger O or N affinity, forming firm Zr-O/Zr-N interactions. The benefit is that the powerful bonding can improve the structure stability in Zr-N-C material wherein the N acts as an anchor to fix the Zr singlet. However, the strong electronic affinity will also produce harsh adsorption ability for other O-containing species during the reaction, hindering the desorption process and hence resulting in inferior reaction activity. As such, external coordination modification is an effective strategy to balance the adsorption/desorption strength of O intermediates.^{20,21} For example, the reaction activity is determined by removing the second *OH intermediate, which demands conquering the large energy barrier due to the strong binding ability of FeN_4 moiety in Fe-N-C.^{22,23} Recent research has demonstrated that the OH group and pyridine molecular can be used to weaken the interaction between the adsorbate and the catalytic surface.^{24,25} Similarly, O species are used near the CoN_4 moiety by controlling the thermal annealing step carefully to optimize the free energy change of the *OOH intermediate.²⁶ It is inspired that each Zr connects with the 6 nearest Zr-N bonds in bulk ZrN, which is different from those for the Fe-N bonds in the Fe_xN ($x = 2-4$, with 3 Fe-N bonds at most) compound. This suggests that the Zr element is prone to form a multi-coordination motif (over 4) intrinsically without sophisticated experimental conditions or skills. A fabricated Zr singlet holds great promise in affordable, long-term stable and high-efficient catalysts, with the virtue of its unique intrinsic multi-coordination pattern.

The key point of the experimental method to prepare atomically dispersed intrinsic multi-coordination Zr lies in forming a homogeneous and well-confined precursor. To do so, we prepared binary Mg-Zr alloys in which Zr atoms are randomly distributed as an atomic solid-solute state in a Mg matrix by an industrial high-energy ball-milling technique.^{27,28} Subsequently, they were pyrolyzed under an atmosphere of mixed CO_2 and NH_3 , and a C-containing template was formed from the Mg matrix, in which the O and N act as effective anchoring bonds for the Zr single atom during the heat treatment process. As a result, an atomically dispersed Zr-N/O-C catalyst is achieved. The as-prepared Zr-N/O-C catalyst with 2.93 wt % metal loading exhibits both high electrochemical catalytic activity and extraordinary long-term structural stability. What is more attractive, the Zn-air battery exhibits a high power density (217.9 mW cm^{-2}) and long cyclability ($>1,000 \text{ h}$) with a low overpotential (0.913 V). Combinations of X-ray absorption near-edge structure (XANES) analysis and density functional theory (DFT) calculations confirm that the outstanding electrocatalytic performance can be attributed to the intrinsic quintuple N and O co-coordination ZrN_4O with 4 in-plane N and an out-of-plane O ligand.

RESULTS

Catalyst synthesis

Atomically dispersed Zr catalysts were synthesized using a ball-milling solid-solution assistant pyrolysis approach, as illustrated in Figure 1A. Specifically, a solid-solution Mg-Zr alloy formed during the high-energy ball-milling pre-treatment, and then the solid-solution Mg-Zr alloy *in situ* changed to a composite single-atom Zr on N and O doping graphene (labeled Zr-N/O-C) in terms of the chemical reaction Mg matrix in a mixed gas environment during the pyrolysis process. Notably, according to the binary Mg-Zr phase diagram, the maximum solubility of Zr in the Mg matrix is $\sim 0.6 \text{ wt } \%$. The broadened peaks and shift to low angles in the Mg-1 wt % Zr alloy reveal that the Zr atoms are well dispersed, revealing the insertion of the larger Zr atom in the Mg matrix ($Mg + Zr \rightarrow MgZr$ [solid solution]). Comparatively, the peak

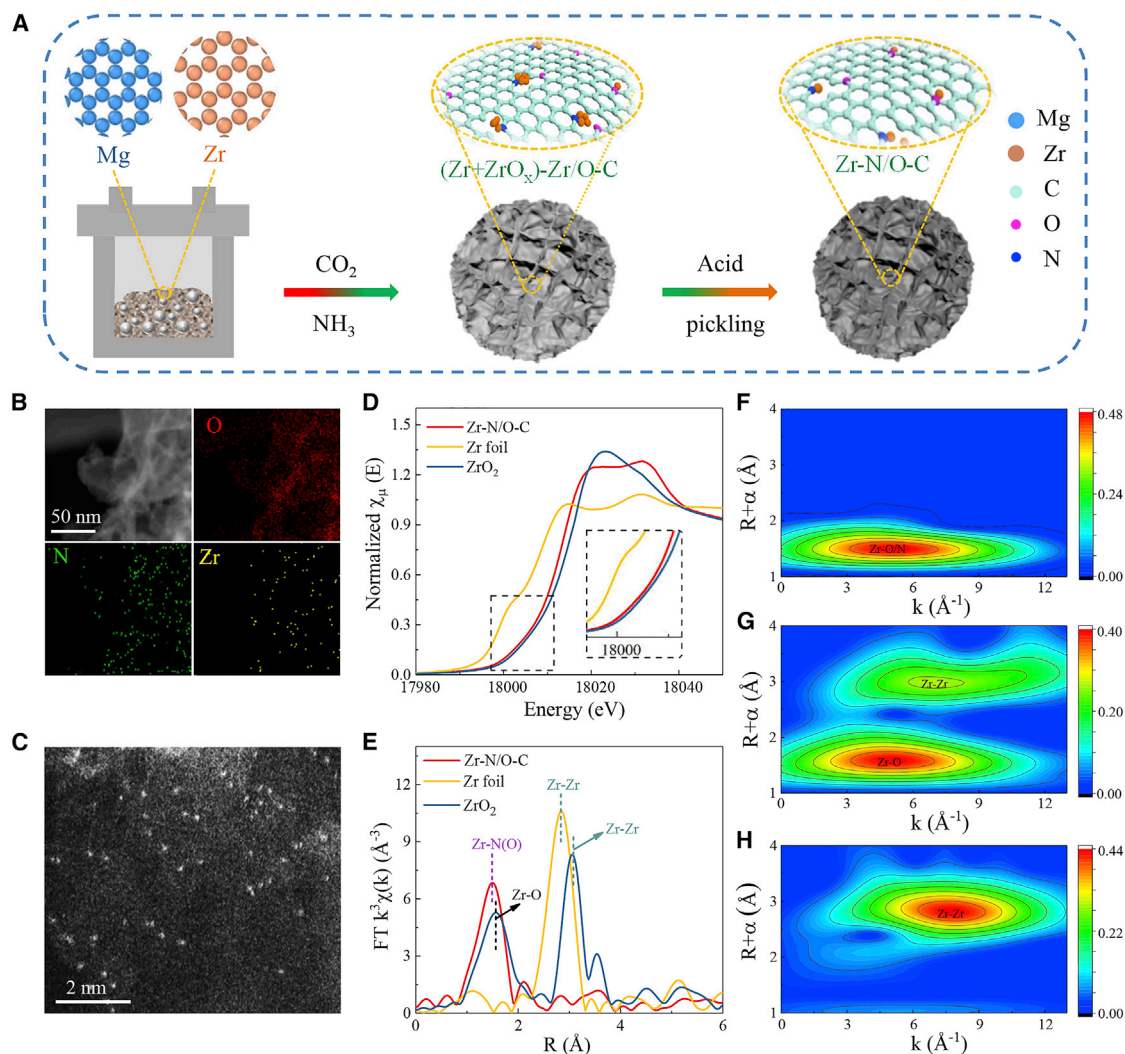
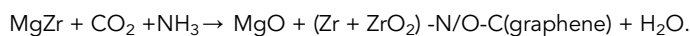


Figure 1. Synthesis and characterization of Zr-N/O-C

- (A) Schematic illustration of the synthesis procedure of atomic-dispersed Zr-N/O-C.
 (B) EDX mapping images of Zr, N, and O.
 (C) HAADF-STEM image of the Zr-N/O-C.
 (D) The experimental Zr K-edge XANES spectra.
 (E) FT k^3 -weighted Zr K-edge EXAFS spectra.
 (F–H) WT-EXAFS plots of Zr-N/O-C, ZrO₂, and Zr foil, respectively.

representing Zr appears when the Zr content increases to 1.5 wt %, indicating that the maximum content of Zr in the Mg matrix is ~ 1 wt % by high-energy ball milling, as evidenced by X-ray diffraction (XRD) patterns (Figure S1A). Simultaneously, the high-angle annular dark-field atomic-resolution-scanning transition electron microscopy (HAADF-STEM) image (Figure S1B) further confirms that the doped Zr atoms are homogeneously constrained by the Mg matrix in Mg-1 wt % Zr alloy.

In addition, the variation of phase composition is investigated by the XRD (Figure S2), in which the Mg matrix has oxidized to MgO and graphene after pyrolysis treatment under CO₂.²⁹ The main chemical process is as follows:



The formation of the *in situ* N-doped graphene inevitably contains defects and/or vacancies because of the lattice mismatch during phase transformation ($\text{Mg} + \text{CO}_2 \rightarrow \text{MgO} + \text{C}[\text{graphene}]$),³⁰ in which it either directly encapsulates Zr atoms in graphene or serves as anchoring sites. Moreover, due to a strong affinity between Zr and N/O, a Zr-N/O-C is formed after removing freestanding oxide residues by hydrofluoric acid (HF) leaching. Experimental condition results show that the reaction of CO_2 reduction by Mg is weak at low temperatures. In turn, the C skeleton tends to collapse under high temperatures. For the mixed ratio of CO_2/NH_3 , excessive CO_2 reacts with Zr to form ZrC, which results in the loss of Zr active sites. Similarly, Zr is prone to convert to ZrN as long as the content of the NH_3 atmosphere is abundant. Consequently, the best-performing Zr-N/O-C catalyst is obtained under the following experimental conditions: the content of 1 wt % Zr, the CO_2/NH_3 gas ratio of 1:0.5, and the temperature of $\sim 900^\circ\text{C}$ (Figure S3). As a reference, a pure N and O doping graphene (N/O-C) has also been prepared using Mg as a precursor.

Atomically dispersed Zr sites

XRD patterns (Figure S4A) do not show characteristic peaks for any crystalline Zr-containing phases or clusters in the Zr-N/O-C catalyst, analogous to that of the N/O-C reference. Raman spectra indicate that the $I_{\text{D}}:I_{\text{G}}$ ratio for the Zr-N/O-C is slightly higher than the N/O-C substrate, revealing that the thin C layer in Zr-N/O-C is more disordered (Figure S4B). Moreover, as confirmed by scanning electron microscopy (SEM) and Brunauer-Emmett-Teller (BET) surface analysis, both N/O-C and Zr-N/O-C show a three-dimensional honeycomb-like morphology, with many gradient macropores in a combination of micropores (Figure S5). Compared with those of the N/O-C reference, the Zr-N/O-C shows a slightly higher specific surface area of $278.80 \text{ m}^2 \text{ g}^{-1}$ and a marginally larger pore volume of $1.15 \text{ cm}^3 \text{ g}^{-1}$. These demonstrate that Zr doping could hardly affect the substrate and macromorphology.

Evidently, inductively coupled plasma atomic emission spectroscopy (ICP-AES, 2.93 wt %; Table S1), energy dispersive X-ray spectroscopy (EDS) (Figure 1B), and quantitative analysis of X-ray photoelectron spectroscopy (XPS) (~ 2.89 wt %; Table S2) confirm the existence of the Zr species, except for C, N, and O. Simultaneously, transmission electron microscopy (TEM) images reveal that neither clusters nor nanoparticles anchor on the substrate of the Zr-N/O-C (Figure S6). In contrast, in the HAADF-STEM image (Figure 1C), a number of bright spots are clearly observed in the Zr-N/O-C, which can be safely attributed to Zr single atoms. The Zr 3d XPS spectra (Figure S7) can be fitted to 2 peaks—Zr-N (180.99 and 183.27 eV) and Zr-O (182.08 and 186.18 eV)—suggesting a dual-ligand configuration with N and O.³¹ The N 1s XPS spectra at 402.51, 400.68 and 398.68 eV are assigned to O-N, C-N, and Zr-N interaction, respectively.³² Based on the XPS peak intensities, the estimated atomic content of Zr-N and Zr-O are 0.094 atom % and 0.024 atom %, respectively, corresponding to an elemental ratio of 4:1 (Table S2).

The Zr K-edge XANES spectra in the Zr-N/O-C is located between the Zr foil and ZrO_2 . The energy region of the Zr-N/O-C shifts slightly (Figures 1D and S8), where the white peak is at a higher energy than the Zr foil but lower than that of ZrO_2 . This observation indicates that the valence state of Zr is positive but lower than 4. The absence of a pre-edge as for a typical MN_4 square planar ($\text{D}_{4\text{h}}$) symmetry demonstrates a different coordination environment of Zr.³³ The Fourier transform of the extended X-ray absorption fine structure (FT-EXAFS) curves (Figure 1E) shows a strong peak at 1.5 Å, which can be assigned to Zr-N-O interaction. The Zr-Zr peak

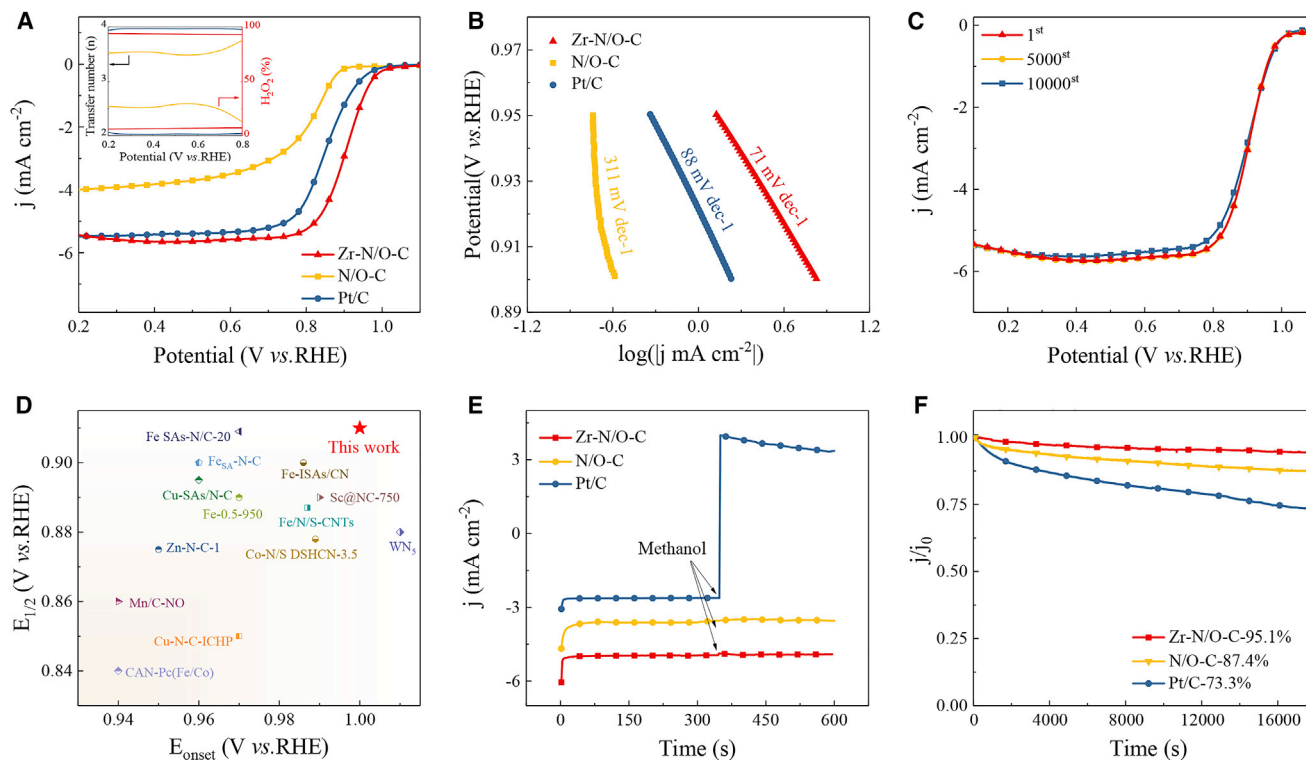


Figure 2. Electrochemical performance of Zr-N/O-C

- (A) LSV curves in O_2 -saturated 0.1 M KOH solutions at a sweep rate of 10 mV s^{-1} . The inset involves peroxide yield and the calculated electron transfer number.
- (B) Tafel slopes of the catalysts.
- (C) LSV curves of Zr-N/O-C before and after accelerated stability tests with 5,000 cycles and 10,000 cycles from 0.2 to 1.1 V (versus RHE) at a sweep rate of 10 mV s^{-1} .
- (D) Contrasting the E_{onset} and $E_{1/2}$ values for Zr-N/O-C and other single-atom catalysts.
- (E) Methanol tolerance test.
- (F) CA test of the catalysts at 0.6 V with 1,600 rpm in O_2 -saturated 0.1 M KOH solutions.

(2.8 Å) is not detected, indicating the absence of near-neighbor Zr. Note that the peak is asymmetrical, with slight variation with a lower k value, implying that additional coordination causes the distortion of Zr atoms out of the graphene plane. The wavelet transform (WT) of the k^3 -weighted EXAFS spectra (Figures 1F–1H) suggests only 1 strong peak at 5 Å^{-1} in the Zr-N/O-C, which can be assigned to the Zr-N/O bond. This contrasts with the ZrO_2 compound and the Zr foil, which show a peak at $\sim 8.2 \text{ Å}^{-1}$, corresponding to the Zr-Zr scattering path. EXAFS fitting (Table S3) indicates that the average Zr-N/O distance is 2.11 Å and the coordination number is close to 5. This structural feature is consistent with the XPS analysis of a ZrN_4O fragment.

Electrochemical performance

To evaluate the electrochemical catalytic performance of the Zr-N/O-C catalysts, catalyst-modified rotating disk electrodes were tested in O_2 - and Ar-saturated 0.1 M KOH solution, respectively, compared with the N/O-C and commercial 20 wt % Pt/C. Cyclic voltammetry (CV) curves display the most positive potential of 0.81 V for the Zr-N/O-C (Figure S9). Linear sweep voltammetry (LSV) results at 1,600 rpm after normalization by glassy carbon (GC) electrodes (Figure 2A) show that the half-wave potential ($E_{1/2} = 0.910 \text{ V}$ versus reversible hydrogen electrode [RHE]) and onset potential ($E_{\text{onset}} = 1.000 \text{ V}$ versus RHE) of the Zr-N/O-C display

the best ORR activity, surpassing that of the N/O-C ($E_{1/2} = 0.805$ V versus RHE, $E_{\text{onset}} = 0.91$ V versus RHE) and commercial Pt/C ($E_{1/2} = 0.851$ V versus RHE, $E_{\text{onset}} = 0.97$ V versus RHE), respectively. This outstanding ORR activity is further identified by the smallest Tafel slopes (Figure 2B)—i.e., 71 mV dec^{-1} (Zr-N/O-C) < 88 mV dec^{-1} (Pt/C) < 311 mV dec^{-1} (N/O-C).

To gain further insight into its catalyst selectivity, we measured the ORR kinetics. The electron-transferring number, detected using rotating ring-disk electrode (RRDE) testing, gives rise to a value of ~ 3.91 (Figure 2A), rendering a Pt-like $4e^-$ reaction mechanism. To estimate potential applications of the Zr-N/O-C electrocatalysis, the stability is tested by conducting accelerated stability tests between 0.8 and 1.1 V versus RHE at 0.1 V s^{-1} in O_2 -saturated 0.1 M KOH solutions. Remarkably, no obvious activity decay is observed for $E_{1/2}$ after 5,000 continuous potential cycles, and only a 5-mV decrease is witnessed after 10,000 continuous potential cycles (Figure 2C), outperforming the recently reported single-atom Co-N-C (8 mV loss).¹⁹ The loss of $E_{1/2}$ for the control catalysts can be ascribed to the presence of nanoclusters (Figure S10) as a result of atom mobility and aggregation after cycles. The highest electrochemical surface area (ECSA) of 74.1 mF cm^{-2} is calculated for the Zr-N/O-C (Figure S11A). Moreover, the Zr-N/O-C exhibits a record-value kinetic current density (j_k) of 28.19 mA cm^{-2} at 0.85 V, which is 20 times higher than that of Pt/C, further confirming its high ORR catalytic activity (Figure S11B). Meanwhile, the turnover frequency (TOF) was calculated to compare the intrinsic activity per active site to other notable catalysts. Intriguingly, Zr-N/O-C exhibited a high TOF of $2.70 \text{ e}^- \text{ site}^{-1} \text{ s}^{-1}$ (0.85 V versus RHE), which is 2.7 times higher than that of commercial Pt/C ($0.98 \text{ e}^- \text{ site}^{-1} \text{ s}^{-1}$). Furthermore, the Zr-N/O-C exhibited higher mass activity (i.e., catalyst mass loading-normalized kinetic current density) and 0.048 times higher intrinsic activity (i.e., the BET surface is a normalized kinetic current density) at 0.85 V versus RHE than those of the N/O-C, confirming the positive effect of the ZrN_4O fragment on intrinsic activity (Figure S11C). It demonstrates that the Zr-N/O-C, compared with literally reported pure non-precious single-atom systems, bestows the highest level of ORR electrocatalysts in terms of $E_{1/2}$ and E_{onset} (Figure 2D; Table S4).

The Poison effect is a critical concern when catalyst acts on the cathode of fuel cell. We tested the methanol crossover effect via the chronoamperometric (CA) responses. The current density of Pt/C drops significantly when methanol is injected into the solution, while that of the Zr-N/O-C and the N/O-C is maintained (Figure 2E). The long-term testing of 16,000 s reveals that only 73.3% remains for Pt/C, while 95.1% is retained for the Zr-N/O-C, followed by the N/O-C (87.4%) (Figure 2F). Poisoning experiments reveal that the Zr-N/O-C is not sensitive to Br^- , Cl^- , and CH_3OH . However, the $E_{1/2}$ exhibits a negative shift by 65 mV in the presence of SCN^- , a commonly adopted ion to Poisson metal sites,^{34,35} implying the ZrN_4O moiety, instead of heterogeneous N or C defects, is the active site (Figure S12).

To assess the performance in a real electrochemical device, the Zr-N/O-C was used in comparison to Pt/C as the cathode in Zn-air batteries (Figures 3A–3C). Not only are high open-circuit voltage of 1.488 V (Figure 3A) and a maximum power density of 217.9 mW cm^{-2} (Figure 3B) achieved but also a longer cycle life (>1,000 h) and a lower charge/discharge overpotential (0.913 V) are delivered to the Zr-N/O-C-based batteries, overwhelming the counterparts equipped with the Pt/C benchmark and other samples (Figure 3C). The rate capability of the Zr-N/O-C (Figure S13A) shows better performance than commercial Pt/C, which emphasizes the good reversibility of the Zr-N/O-C. What is more attractive is that this high performance can also be

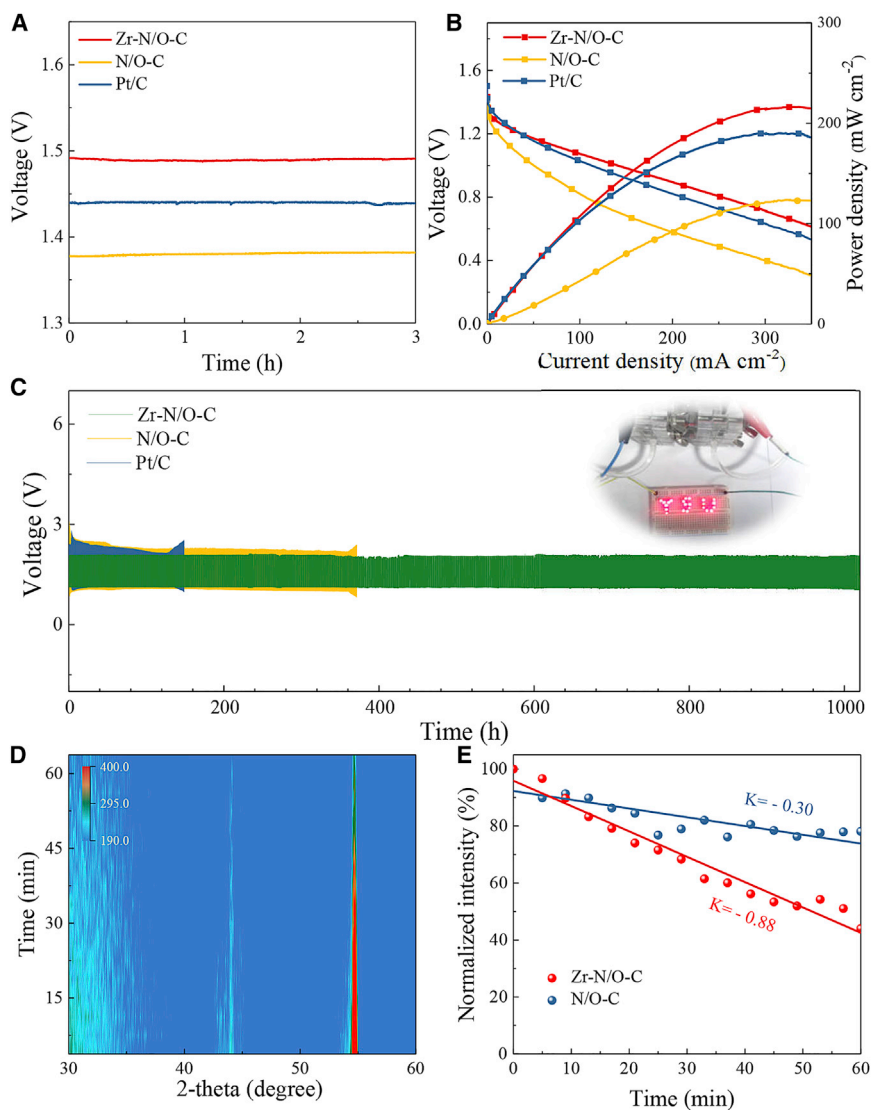


Figure 3. The performance of Zn-air batteries

- (A) Open circuit voltage curves.
 (B) Discharge polarization curves and corresponding power density plots.
 (C) Long-term discharge/charge cycling performance.
 (D) *In situ* XRD contour plots of Zn-air batteries with the Zr-N/O-C electrodes during discharge.
 (E) Intensity changes of C peak at 55° of different air cathodes during Zn-air battery operation.

achieved in the temperature range of -10°C to 50°C , illustrating its promise for wide-temperature industrial applications (Figures S13B and S13C). In addition, this high ORR activity has been clarified further by *in situ* XRD measures on Zn-air batteries assembled in a tailor-made mold (Figures 3D, 3E, and S14). Initially, 2 major peaks of C at 44°C and 55°C were observed for both the Zr-N/O-C and the N/O-C. It became weak gradually during the discharging procedure, which can be attributed to the continuous adsorbed O molecular on the cathode surface during the ORR process.³⁶ A more negative slope (-0.88) of the Zr-N/O-C compared with the N/O-C electrode (Figure 3E) suggests a more efficient ORR activity. In fact, the deposition of ZnO would gradually clog active sites and hamper O₂ diffusion, resulting in the degradation of the discharge performance. However, no ZnO

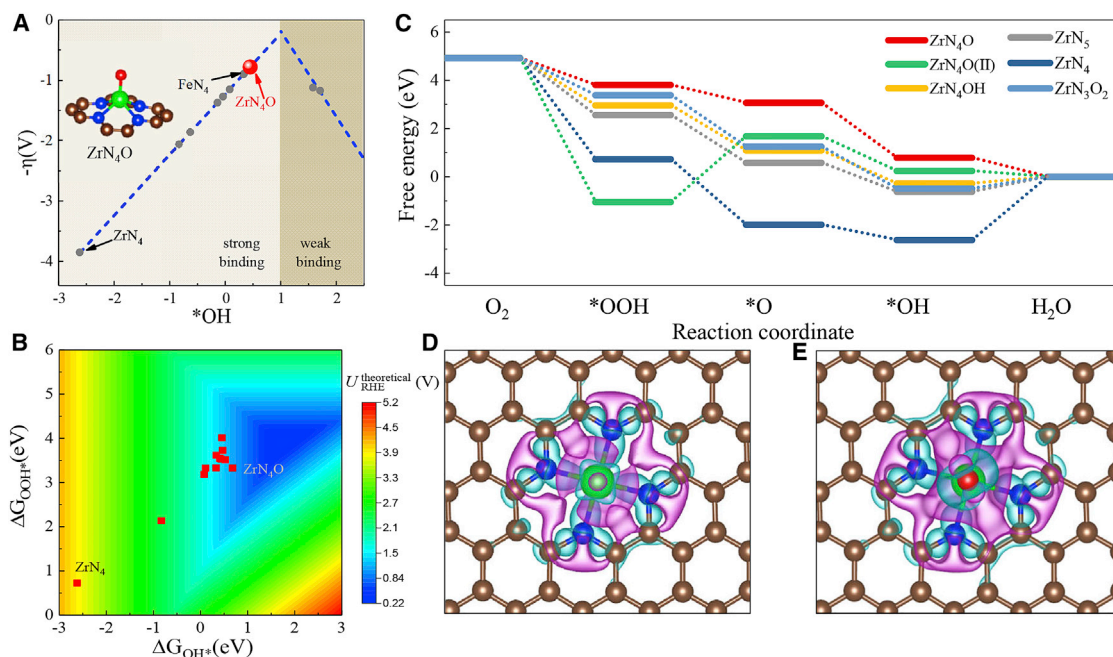


Figure 4. Theoretical interpretation

(A) Calculated catalytic activity volcano plots. The inset corresponds to ZrN_4O moiety.
 (B) Color-filled contour plots of the activity as the function of both $\Delta G_{^*OOH}$ and $\Delta G_{^*OH}$.
 (C) Free energy diagram.
 (D and E) Differential charge densities of ZrN_4 and ZrN_4O moieties, respectively.

signal is captured during the whole steady discharge plateaus process, confirming the completely suppressed metal oxidation on the cathode.

Catalytic mechanism

To characterize the nature of the reaction center, DFT calculations were performed. Various possible reaction center configurations (ZrN_4 , ZrN_4O , ZrN_3O_2 , ZrN_5 , $ZrNO_4$, $ZrN_4O(II)$, and ZrN_4OH) and their ORR activities were investigated (Figure S15). The performances were compared with a literally well-studied FeN_4 moiety.¹⁴ The results show that the bare ZrN_4 moiety is not reactive with a severe overpotential, emphasizing an endothermic reaction (Figure 4A). The performance gradually increased and an obvious improvement was achieved for ZrN_4O moiety, with a smaller overpotential than that of the FeN_4 fragment, wherein the metal was confined by 4 in-plane N atoms and 1 out-of-plane O atom.

To further investigate the catalytic performance, we calculated the adsorption energy of the key reaction intermediates (*OOH , *O , and *OH). For a family of catalysis, a linear relationship of $\Delta G_{^*OOH}/\Delta G_{^*O}$ and $\Delta G_{^*OH}$ can be plotted (Figure S16). Based on the relationship, the reaction activity can be derived as the function of both $\Delta G_{^*OH}$ and $\Delta G_{^*OOH}$, which is of great significance in understanding the reaction mechanism.³⁷ As displayed in Figure 4B, the closer to the corner of the square, the worse the activity because of the poor adsorption of the intermediates.⁹ Specifically, ZrN_4 moiety is located on the bottom left, demonstrating poor adsorption of neither *OOH nor *OH . This is consistent with the volcano plot, in which most dots scatter on the strong interaction side, with $\Delta G_{^*OH}$ less than 0.5 eV. Also, from the free energy diagram (Figure 4C), the intense binding of *OH makes the last step ($^*OH \rightarrow H_2O$) an uphill step, which is thus the potential determining step (PDS). By contrast, with varying functional groups, the

adsorption of reaction intermediates is adjusted, and the points move to the light-blue triangle region, where all of the ΔG s tend to be optimal. Specifically, the $\Delta G_{*_{\text{OH}}}$ for Zr-N/O-C with ZrN_4O motif turns downhill ($\Delta G_{*_{\text{OH}}} = 0.45$ eV), giving rise to an overpotential of 0.78 V. We also noticed that when the metal attached by another OH group or the C substrate is oxidized by O, the ZrN_4O fragment remains, with even smaller overpotential (Figure 4A), which occurs in the aqueous/alkaline solution or in high-temperature pyrolysis by chance.

We also performed differential charge density calculations to better understand the above variation of free energy (Figures 4D and 4E). Compared with ZrN_4 , the charge depletion on the metal of the unsaturated dual-ligand confining ZrN_4O structure is more obvious, which gives rise to a smaller electron population on the metal. The O atom is an electron-withdrawing function group, and the accumulation of charge is witnessed on the O atom. Subsequently, the Zr 4d state is shifted downward as electron density is decreased (Figure S17). According to the d-band center theory,³⁸ the position of the d-band is linearly related to the adsorption free energy. More specifically, the position of the d-band down from the Fermi level is lower, and the adsorption becomes weaker. As a result, the ZrN_4 is in the poor-adsorption energy region, whereas the ZrN_4O structure is close to the optimal center, with favorable reactant-binding energy.

DISCUSSION

In summary, an atomically dispersed intrinsic quintuple N- and O-coordinated Zr-N/O-C catalyst has been fabricated through a ball-milling, solid-solution assisted pyrolysis approach. ZrN_4O moieties were verified using XAS, HAADF-STEM imaging, and the DFT model. The Zr-N/O-C catalyst exhibits both high half-wave potential ($E_{1/2} = 0.910$ V versus RHE) and onset potential ($E_{\text{onset}} = 1,000$ V vs. RHE) in an alkaline solution, which also has an ultra-high selectivity for a $4e^-$ reduction pathway, good methanol tolerance, and extraordinary long-term stability. Moreover, the Zn-air batteries exhibit high comprehensive electrochemical properties in a wide temperature range of -10°C to 50°C , overwhelming the counterparts equipped with the Pt/C benchmark and other similar catalysts. Taking into account its simple process, low cost, and high catalytic activity, the work provides a new way to develop large-scale non-noble metal catalysts in a new generation of sustainable energy devices.

EXPERIMENTAL PROCEDURES

Resource availability

Lead contact

All queries should be directed to Qiuming Peng (pengqiuming@ysu.edu.cn).

Materials availability

This study did not generate new unique materials.

Data and code availability

The authors declare that the data supporting the findings of this study are available within the article and the [supplemental information](#). All other data are available from the lead contact upon reasonable request.

Preparation of Zr-N/O-C

The mixed pure Mg and Zr powders (1 wt % Zr, thereafter in wt %) were treated by ball milling. A total of 495 g Mg and 5 g Zr powder was poured into a stainless-steel tank, along with 10 stainless-steel balls 5 mm in diameter and 40 stainless-steel balls 3 mm in diameter. This powder mixture was then ball milled at 800 rpm, with 20 consecutive cycles of 30-min segments and 10-min cool-down periods. The powder

mixture was then pyrolyzed at 800°C–1,000°C under a CO₂/NH₃ (1:0.2, 1:0.5, and 1:0.8) atmosphere for 5 h, with a heating rate of 5°C min⁻¹ in the subsequent process. Finally, Zr-N/O-C is obtained after an acid leaching treatment in a 10% HF solution for 8 h to removing freestanding oxide. N/O-C was synthesized with the same procedure; however, Mg powders were used instead of Mg-1 wt % Zr.

Material characterization

XRD (D8, Brook) measurements were performed using a powder with Cu K α radiation ($\lambda = 1.5406 \text{ \AA}$) in a 2θ range from 20° to 60°, with a scanning rate of 4° min⁻¹. The morphologies were investigated with high-resolution TEM (HRTEM)-STEM (JEOL2100; G2: an ultra-high point resolution of 0.1 nm with a Gatan Model-994 CCD digital camera and electron energy-loss spectroscopy [EELS], operated at a voltage of 300 kV). XPS (ThermoFisher) was performed using Al K α radiation. XAS was collected on the beamline BL07A1 in NSRRC (National Synchrotron Radiation Research Center). The radiation was monochromatized by a Si(111) double-crystal monochromator. The acquired EXAFS data were processed according to the standard procedures using the ATHENA module implemented in the IFEFFIT software packages. XANES and EXAFS data reduction and analysis were processed by Athena software.³⁹ The $\chi_{(k)}$ data were Fourier transformed to real (R) space using a Hann window ($d_k = 1.0 \text{ \AA}^{-1}$) to separate the EXAFS contributions from different coordination shells. The quantitative information is obtained by the least-squares curve fitting in the R space with a Fourier transform k space range of 2.0–15 \AA^{-1} , using the module ARTEMIS in IFEFFIT. The backscattering amplitude $F_{(k)}$ and phase shift $\phi_{(k)}$ were calculated using FEFF8.0 code.

Electrochemical tests

ORR electrochemical measurements were carried out in a 3-electrode system using an RRDE-3A with an electrochemical workstation (CHI 760E). GC with a diameter of 4 mm was used as the support for the working electrode. A graphite rod was used as the counter electrode instead of Pt to prevent pollution from long-term electrochemical corrosion. The reference electrode was Ag/AgCl (filled with saturated KCl solution) electrode. All of the potentials were calibrated to RHE potential calculated from the equation

$$E(\text{vs. RHE}) = E(\text{vs. Ag/AgCl}) + 0.198\text{V} + 0.059 \times \text{pH}.$$

All of the potentials in this study are quoted against RHE. The catalysts' ink was fabricated by mixing catalyst powder (4 mg) with a mixture of 200 μL isopropanol, 800 μL H₂O, and 20 μL Nafion solution under ultrasonic conditions for 30 min. The ink was drop-cast on the disk electrode with a controlled loading of 0.339 mg cm⁻² and dried at room temperature to yield a thin film electrode.

Before the measurement, a stream of Ar or O₂ flow was delivered to the electrolyte for 30 min to obtain an Ar- or O₂-saturated solution. The ORR curve was acquired under O-saturated conditions by subtracting the data under Ar-saturated conditions as a background. CV measurements were carried out in Ar- or O₂-saturated 0.1 M KOH solutions at a scanning rate of 50 mV s⁻¹ in a cycling potential between 0 and 1.2 V versus RHE. The catalytic activity of samples was evaluated by using LSV at scan rate of 10 mV s⁻¹ with different rotation rates (400–2,000 rpm).

For the ORR at an RRDE, the electron transferred number (n) and kinetic current density (j_k) were calculated according to the Koutecky-Levich (K-L) plot linear fit lines from the K-L equation:⁴⁰

$$\frac{1}{j} = \frac{1}{j_L} + \frac{1}{j_k} = \frac{1}{B\omega^{1/2}} + \frac{1}{j_k}$$

$$B = 0.62nFD_0^{2/3}v^{-1/6}C_0$$

where j was the current density measured from the ORR, j_L and j_k represented the diffusion limiting and the kinetic current density individually, ω was the angular velocity of the disk, F was the Faraday constant ($F = 96,485 \text{ C mol}^{-1}$), D_0 was the diffusion coefficient of O_2 ($1.9 \times 10^{-5} \text{ cm}^2 \text{ s}^{-1}$), C_0 was the bulk concentration of O_2 ($1.2 \times 10^{-6} \text{ mol cm}^{-3}$), and v was the kinematic viscosity of the electrolyte ($0.01 \text{ cm}^2 \text{ s}^{-1}$). For the RRDE tests, the hydrogen peroxide yield (H_2O_2 [%]) and the electron transfer number (n) can be calculated from the LSV at 1,600 rpm using the following equation:

$$\text{H}_2\text{O}_2(\%) = 200 \times \frac{I_r}{I_d + \frac{I_r}{N}}$$

$$n = 4 \times \frac{I_d}{I_d + \frac{I_r}{N}}$$

where I_d was the disk current, I_r was the ring current, and N was the current collection efficiency of the Pt ring with a value of 0.4.

Zn-air battery tests

The temperature was controlled by a programmable box (GDJS-100, Beijing YaShiLin Testing Equipment). A total of 6 M KOH with 0.2 M $\text{Zn}(\text{CH}_3\text{COOH})_2$ was the electrolyte, while the polished Zn plate was used as the anode. Homogeneous catalyst ink consists of the nanocomposites, ionomer (Nafion solution, 5 wt %), isopropanol, and H_2O . The air cathode was made by drop casting the catalyst ink onto hydrophilic carbon paper (HESEN HCP120) with a loading of 1.0 mg cm^{-2} . The polarization curves were obtained using a CHI760E electrochemical workstation (Shanghai Chenhua Instrument), and the galvanostatic charge-discharge tests were performed on a battery measurement system (Land CT2001A).

In situ XRD characterization of Zn-air battery

In situ XRD measurements were obtained with an X-ray powder diffractometer (D8 ADVANCE, Bruker AXS GmbH). The Zn-air battery was assembled using a tailor-made mold with a window for X-ray penetration. The constant galvanostatic discharge curve of the Zn-air battery was measured by the CHI660E (Shanghai Chenhua Instrument) electrochemical workstation, and the current density was 10 mA cm^{-2} . The XRD pattern recording frequency was 10 min for the same position.

Computational methods

All of the calculations were performed using the projector-augmented wave method as implemented in the Vienna *ab initio* simulation package (VASP).^{41,42} The exchange-correlation potentials were treated in the generalized gradient approximation by the Perdew-Burke-Ernzerhof form.^{43–45} The energy cutoff of 500 eV was set for the plane-wave expansion. All of the structural relaxations were performed until the Hellmann-Feynman forces were $<10^{-5} \text{ eV/\AA}$. Brillouin zone with a Gaussian broadening of 0.05 eV was performed. The centered Monkhorst-Pack k-point meshes for sampling the Brillouin zone was $5 \times 5 \times 1$. The van der Waals (vdW) interaction was involved via the semi-empirical DFT-D2 field method.²⁶ The Gibbs free energy was calculated as follows:

$$\Delta G = \Delta E + \Delta ZPE - T\Delta S,$$

where ΔE was the DFT calculated adsorption energy difference from the initial to the final states. ΔZPE was the change in zero-point energy (ZPE). T was fixed at 289.15 K in our study and ΔS was the entropy change. The nature of the stationary point and ZPE corrections was characterized by calculating the harmonic vibration frequency. The Gibbs free energy change (ΔG_i , $i = 1-4$) for each elementary step can be summarized as follows:

$$\Delta G_1 = 4.92 - \Delta G_{*OOH}$$

$$\Delta G_2 = \Delta G_{*OOH} - \Delta G_{*O}$$

$$\Delta G_3 = \Delta G_{*O} - \Delta G_{*OH}$$

$$\Delta G_4 = \Delta G_{*OH}$$

The theoretical overpotential η^{ORR} for a given electrocatalyst can be evaluated as

$$\eta^{\text{ORR}} = 1.23 \text{ V} - \min\{\Delta G_1, \Delta G_2, \Delta G_3, \Delta G_4\}/e.$$

SUPPLEMENTAL INFORMATION

Supplemental information can be found online at <https://doi.org/10.1016/j.xcrp.2022.100773>.

ACKNOWLEDGMENTS

We greatly acknowledge the financial support from the National Natural Science Foundation (51971194 and 52171126), the NSF (no. 2021203005), and the Top Young Scholars Foundation (BJ2021042). We would like to express our gratitude to the Ministry of Education Yangtze River Scholar professor program (T2020124). J.W. and J.S.T. wish to thank Compute Canada for the allocation of computer resources. J.S.T. is supported by an NSERC (Natural Sciences and Engineering Research Council of Canada) Discovery Grant.

AUTHOR CONTRIBUTIONS

Q.P. conceived the project. X.Z., J.W., M.Y., and G.Z. carried out the syntheses and structural characterizations. X.Z. conducted the electrochemical reduction experiments. J.W. provided the XANES and EXAFS analyses. C.Y. and G.Z. carried out the *in situ* XRD experiment and provided the analysis. J.W. and J.S.T. carried out the computational investigation and provided the theoretical analysis. C.F. helped to write this manuscript. Q.P. was responsible for the overall direction of the project. All of the other authors participated in preparing the manuscript and contributed to the discussion.

DECLARATION OF INTERESTS

The authors declare no competing interests.

Received: November 10, 2021

Revised: December 10, 2021

Accepted: January 25, 2022

Published: March 16, 2022

REFERENCES

- Deng, Y.P., Jiang, Y., Liang, R., Zhang, S.J., Luo, D., Hu, Y., Wang, X., Li, J.T., Yu, A., and Chen, Z. (2020). Dynamic electrocatalyst with current-driven oxyhydroxide shell for rechargeable zinc-air battery. *Nat. Commun.* **11**, 1952.
- Zhang, J., Zhao, Z., Xia, Z., and Dai, L. (2015). A metal-free bifunctional electrocatalyst for oxygen reduction and oxygen evolution reactions. *Nat. Nanotechnol.* **10**, 444–452.
- Li, Y., Gong, M., Liang, Y., Feng, J., Kim, J.E., Wang, H., Hong, G., Zhang, B., and Dai, H. (2013). Advanced zinc-air batteries based on high-performance hybrid electrocatalysts. *Nat. Commun.* **4**, 1805.
- Cano, Z.P., Banham, D., Ye, S., Hintennach, A., Lu, J., Fowler, M., and Chen, Z. (2018). Batteries and fuel cells for emerging electric vehicle markets. *Nat. Energy* **3**, 279–289.
- Lee, J.S., Kim, S.T., Cao, R., Choi, N.S., Liu, M., Lee, K.T., and Cho, J. (2011). Metal-air batteries with high energy density: Li-air versus Zn-air. *Adv. Energy Mater.* **1**, 34–50.
- Tang, C., Wang, H.F., and Zhang, Q. (2018). Multiscale principles to boost reactivity in gas-involving energy electrocatalysis. *Acc. Chem. Res.* **51**, 881–889.
- Wu, G., and Zelenay, P. (2013). Nanostructured nonprecious metal catalysts for oxygen reduction reaction. *Acc. Chem. Res.* **46**, 1878–1889.
- Li, Y., Zhou, W., Wang, H., Xie, L., Liang, Y., Wei, F., Idrobo, J.C., Pennycook, S.J., and Dai, H. (2012). An oxygen reduction electrocatalyst based on carbon nanotube-graphene complexes. *Nat. Nanotechnol.* **7**, 394–400.
- Bashyam, R., and Zelenay, P. (2006). A class of non-precious metal composite catalysts for fuel cells. *Nature* **443**, 63–66.
- Banham, D., Ye, S., Pei, K., Ozaki, J.i., Kishimoto, T., and Imashiro, Y. (2015). A review of the stability and durability of non-precious metal catalysts for the oxygen reduction reaction in proton exchange membrane fuel cells. *J. Power Sources* **285**, 334–348.
- Shao, Y., Dodelet, J.P., Wu, G., and Zelenay, P. (2019). PGM-free cathode catalysts for PEM fuel cells: a mini-review on stability challenges. *Adv. Mater.* **31**, 1807615.
- Choi, C.H., Baldizzone, C., Grote, J.P., Schuppert, A.K., Jaouen, F., and Mayrhofer, K.J.J. (2015). Stability of Fe-N-C catalysts in acidic medium studied by operando spectroscopy. *Angew. Chem. Int. Ed.* **54**, 12753–12757.
- Wang, X.X., Cullen, D.A., Pan, Y.T., Hwang, S., Wang, M., Feng, Z., Wang, J., Engelhard, M.H., Zhang, H., He, Y., et al. (2018). Nitrogen-coordinated single cobalt atom catalysts for oxygen reduction in proton exchange membrane fuel cells. *Adv. Mater.* **30**, 1706758.
- Ferrandon, M., Wang, X., Kropf, A.J., Myers, D.J., Wu, G., Johnston, C.M., and Zelenay, P. (2013). Stability of iron species in heat-treated polyaniline-iron-carbon polymer electrolyte fuel cell cathode catalysts. *Electrochim. Acta* **110**, 282–291.
- Ahn, S.H., Yu, X., and Manthiram, A. (2017). "Wiring" Fe-N_x-embedded porous carbon framework onto 1D nanotubes for efficient oxygen reduction reaction in alkaline and acidic media. *Adv. Mater.* **29**, 1606534.
- Jiang, W.J., Gu, L., Li, L., Zhang, Y., Zhang, X., Zhang, L.J., Wang, J.Q., Hu, J.S., Wei, Z., and Wan, L.J. (2016). Understanding the high activity of Fe-N-C electrocatalysts in oxygen reduction: Fe/Fe₃C nanoparticles boost the activity of Fe-N_x. *J. Am. Chem. Soc.* **138**, 3570–3578.
- Chen, J., Li, H., Fan, C., Meng, Q., Tang, Y., Qiu, X., Fu, G., and Ma, T. (2020). Dual single-atomic Ni-N₄ and Fe-N₄ sites constructing Janus hollow graphene for selective oxygen electrocatalysis. *Adv. Mater.* **32**, 2003134.
- Li, J., Chen, M., Cullen, D.A., Hwang, S., Wang, M., Li, B., Liu, K., Karakalos, S., Lucero, M., Zhang, H., et al. (2018). Atomically dispersed manganese catalysts for oxygen reduction in proton-exchange membrane fuel cells. *Nat. Catal.* **1**, 935–945.
- Xie, X., He, C., Li, B., He, Y., Cullen, D.A., Wegener, E.C., Kropf, A.J., Martinez, U., Cheng, Y., Engelhard, M.H., et al. (2020). Performance enhancement and degradation mechanism identification of a single-atom Co-N-C catalyst for proton exchange membrane fuel cells. *Nat. Catal.* **3**, 1044–1054.
- Chen, Z., Huang, A., Yu, K., Cui, T., Zhuang, Z., Liu, S., Li, J., Tu, R., Sun, K., and Tan, X. (2021). Fe₁N₄-O₁ site with axial Fe-O coordination for highly selective CO₂ reduction over a wide potential range. *Energy Environ. Sci.* **14**, 3430–3437.
- Cao, R., Thapa, R., Kim, H., Xu, X., Kim, M.G., Li, Q., Park, N., Liu, M., and Cho, J. (2013). Promotion of oxygen reduction by a bio-inspired tethered iron phthalocyanine carbon nanotube-based catalyst. *Nat. Commun.* **4**, 2076.
- Chen, K., Liu, K., An, P., Li, H., Lin, Y., Hu, J., Jia, C., Fu, J., Li, H., and Liu, H. (2020). Iron phthalocyanine with coordination induced electronic localization to boost oxygen reduction reaction. *Nat. Commun.* **11**, 4173.
- Li, L., Huang, B., Tang, X., Hong, Y., Zhai, W., Hu, T., Yuan, K., and Chen, Y. (2021). Recent developments of microenvironment engineering of single-atom catalysts for oxygen reduction toward desired activity and selectivity. *Adv. Funct. Mater.* **31**, 2103857.
- Wan, C., Duan, X., and Huang, Y. (2020). Molecular design of single-atom catalysts for oxygen reduction reaction. *Adv. Energy Mater.* **10**, 1903815.
- Zhang, H., Li, J., Xi, S., Du, Y., Hai, X., Wang, J., Xu, H., Wu, G., Zhang, J., Lu, J., and Wang, J. (2019). A graphene-supported single-atom FeN₅ catalytic site for efficient electrochemical CO₂ reduction. *Angew. Chem. Int. Ed.* **58**, 14871–14876.
- Jung, E., Shin, H., Lee, B.-H., Efremov, V., Lee, S., Lee, H.S., Kim, J., Antink, W.H., Park, S., and Lee, K.S. (2020). Atomic-level tuning of Co-N-C catalyst for high-performance electrochemical H₂O₂ production. *Nat. Mater.* **19**, 436–442.
- Zghal, S., Hytch, M., Chevalier, J.P., Twisten, R., Wu, F., and Bellon, P. (2002). Electron microscopy nanoscale characterization of ballmilled Cu-Ag powders. Part I: solid solution synthesized by cryo-milling. *Acta Mater.* **50**, 4695–4709.
- Aureli, M., Doumanidis, C.C., Gunduz, I.E., Hussien, A.G.S., Liao, Y., Rebholz, C., and Doumanidis, C.C. (2017). Mechanics and energetics modeling of ball-milled metal foil and particle structures. *Acta Mater.* **123**, 305–316.
- Chakrabarti, A., Lu, J., Skrabutenas, J.C., Xu, T., Xiao, Z., Maguire, J.A., and Hosmane, N.S. (2011). Conversion of carbon dioxide to few-layer graphene. *J. Mater. Chem.* **21**, 9491–9493.
- Zhang, Y., Deng, S., Luo, M., Pan, G., Zeng, Y., Lu, X., Ai, C., Liu, Q., Xiong, Q., and Wang, X. (2019). Defect promoted capacity and durability of N-MnO_{2-x} branch arrays via low-temperature NH₃ treatment for advanced aqueous zinc ion batteries. *Small* **15**, 1905452.
- Yuan, Y., Wang, J., Adimi, S., Shen, H., Thomas, T., Ma, R., Atfield, J.P., and Yang, M. (2020). Zirconium nitride catalysts surpass platinum for oxygen reduction. *Nat. Mater.* **19**, 282–286.
- Chen, Y., Ji, S., Zhao, S., Chen, W., Dong, J., Cheong, W.-C., Shen, R., Wen, X., Zheng, L., and Rykov, A. (2018). Enhanced oxygen reduction with single-atomic-site iron catalysts for a zinc-air battery and hydrogen-air fuel cell. *Nat. Commun.* **9**, 1–12.
- Jiang, R., Li, L., Sheng, T., Hu, G., Chen, Y., and Wang, L. (2018). Edge-site engineering of atomically dispersed Fe-N₄ by selective C-N bond cleavage for enhanced oxygen reduction reaction activities. *J. Am. Chem. Soc.* **140**, 11594–11598.
- Liu, S., Li, Z., Wang, C., Tao, W., Huang, M., Zuo, M., Yang, Y., Yang, K., Zhang, L., and Chen, S. (2020). Turning main-group element magnesium into a highly active electrocatalyst for oxygen reduction reaction. *Nat. Commun.* **11**, 1–11.
- Jia, Y., Zhang, L., Zhuang, L., Liu, H., Yan, X., Wang, X., Liu, J., Wang, J., Zheng, Y., Xiao, Z., et al. (2019). Identification of active sites for acidic oxygen reduction on carbon catalysts with and without nitrogen doping. *Nat. Catal.* **2**, 688–695.
- Wang, M., Wang, W., Qian, T., Liu, S., Li, Y., Hou, Z., Goodenough, J.B., Ajayan, P.M., and Yan, C. (2019). Oxidizing vacancies in nitrogen-doped carbon enhance air-cathode activity. *Adv. Mater.* **31**, 1803339.
- Cai, Y., Fu, J., Zhou, Y., Chang, Y.C., Min, Q., Zhu, J.J., Lin, Y., and Zhu, W. (2021). Insights on forming N,O-coordinated Cu single-atom catalysts for electrochemical reduction CO₂ to methane. *Nat. Commun.* **12**, 586.
- Norskov, J.K., Abild-Pedersen, F., Studt, F., and Bligaard, T. (2011). Density functional theory in surface chemistry and catalysis. *Proc. Natl. Acad. Sci.* **108**, 937–943.

39. Ravel, B., Ravel, B., and Newville, M. (2005). ATHENA, ARTEMIS, HEPHAESTUS: data analysis for X-ray absorption spectroscopy using IFEFFIT. *J. Synchrotron Radiat.* *12*, 537–541.
40. Gao, R., Wang, J., Huang, Z.F., Zhang, R., Wang, W., Pan, L., Zhang, J., Zhu, W., Zhang, X., Shi, C., et al. (2021). Pt/Fe₂O₃ with Pt–Fe pair sites as a catalyst for oxygen reduction with ultralow Pt loading. *Nat. Energy* *6*, 614–623.
41. Blöchl, P.E. (1994). Projector augmented-wave method. *Phys. Rev. B* *50*, 17953.
42. Kresse, G., and Furthmüller, J. (1996). Efficient iterative schemes for ab initio total-energy calculations using a plane-wave basis set. *Phys. Rev. B* *54*, 11169.
43. Perdew, J.P., Burke, K., and Ernzerhof, M. (1996). Generalized gradient approximation made simple. *Phys. Rev. Lett.* *77*, 3865.
44. Hohenberg, P., and Kohn, W. (1964). Density functional theory. *J. Phys. Rev.* *136*, B864.
45. Kohn, W., and Sham, L.J. (1965). Self-consistent equations including exchange and correlation effects. *Phys. Rev. B* *140*, A1133.

Cell Reports Physical Science, Volume 3

Supplemental information

**Atomically dispersed quintuple nitrogen and oxygen
co-coordinated zirconium on graphene-type substrate
for highly efficient oxygen reduction reaction**

Xue Zhao, Jing Wang, Jinming Wang, Meng Yang, Chenglin Yan, Guodong Zou, John S. Tse, Carlos Fernandez, and Qiuming Peng

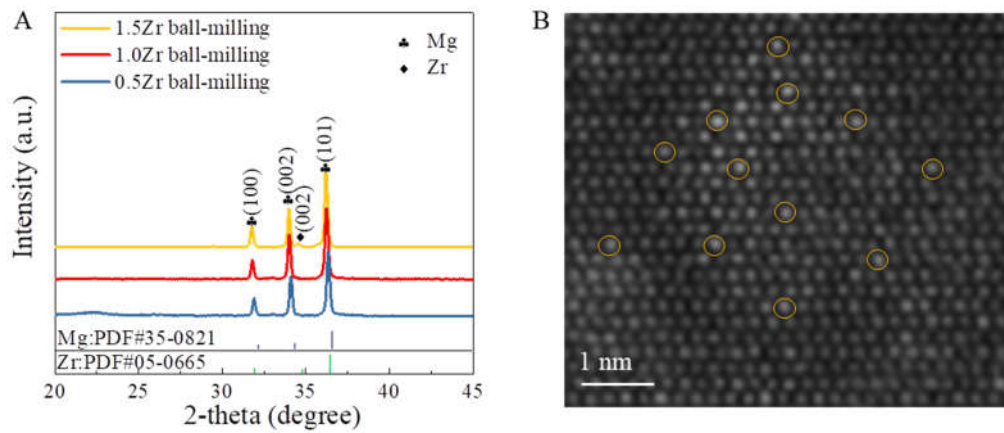


Figure S1 (A) XRD patterns of the samples. Ball milled Mg-1.5Zr Mg-1Zr and Mg-0.5Zr before pyrolysis. **(B)** HAADF-STEM image of the Mg-1Zr, the bright dots are Zr atoms, and the slightly darker dots are Mg atoms.

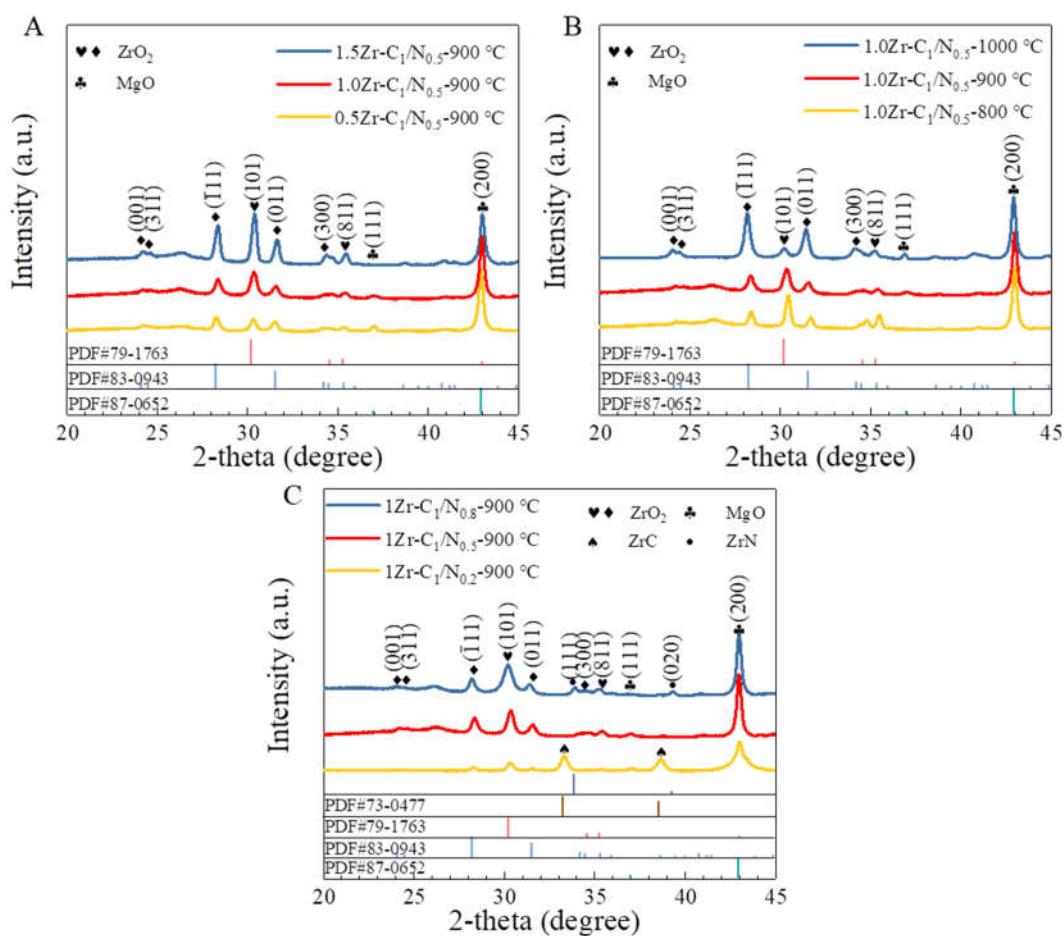


Figure S2 (A) XRD patterns of the Mg-1.5Zr Mg-1Zr and Mg-0.5Zr after pyrolyzed in the mixing gas of CO₂:NH₃=(1:0.5) at 900 °C. **(B)** XRD patterns of different Mg-1Zr samples. The samples were pyrolyzed at 800, 900 and 1000 °C under the mixing gas of CO₂:NH₃=(1:0.5) atmosphere, respectively. **(C)** XRD patterns of different Mg-1Zr samples. The samples were pyrolyzed at 900 °C under the mixing gas of CO₂:NH₃=(1:0.2), CO₂:NH₃=(1:0.5) and CO₂:NH₃=(1:0.8) atmosphere, respectively.

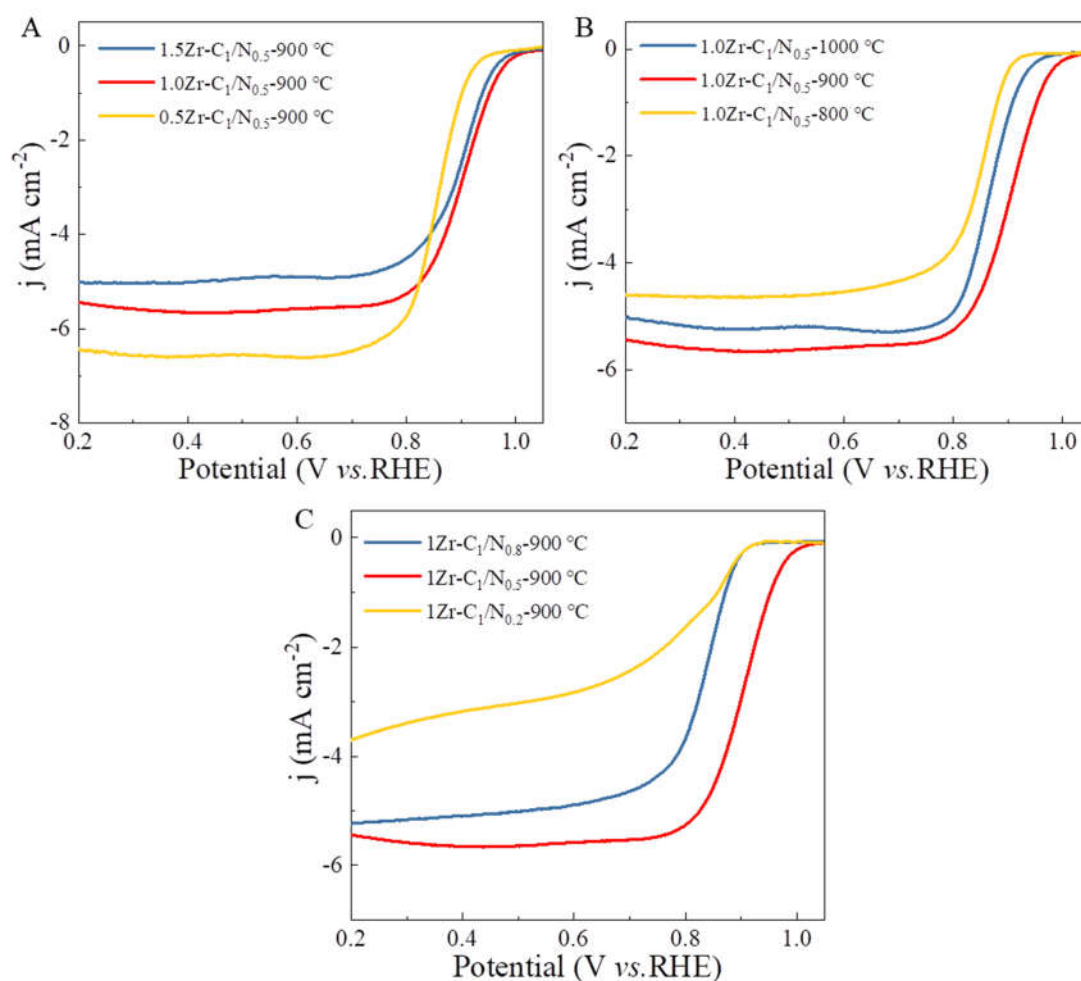


Figure S3 (A) LSV curves of the Mg-1.5Zr, Mg-1Zr and Mg-0.5Zr after pickling in the mixing gas of CO₂:NH₃=(1:0.5) at 900 °C. (B) LSV curves of Mg-1Zr samples pyrolyzed at 800, 900 and 1000 °C under the mixing gas of CO₂:NH₃=(1:0.5) atmosphere, respectively. (C) LSV curves of different Mg-1Zr samples pyrolyzed under the mixing gas of CO₂:NH₃=(1:0.2), CO₂:NH₃=(1:0.5) and CO₂:NH₃=(1:0.8) atmosphere, respectively, with temperature at 900 °C.

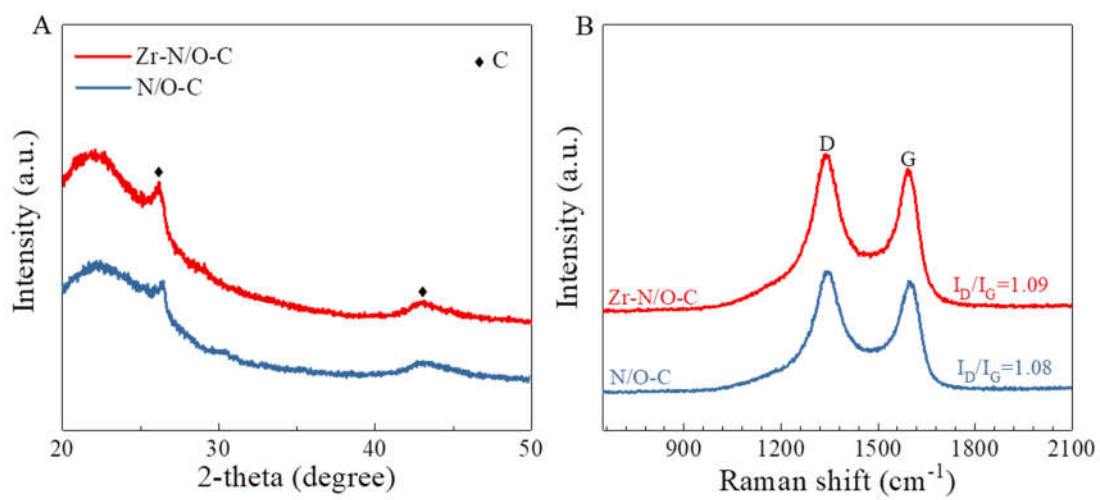


Figure S4 XRD and Raman patterns of the Zr-N/O-C and N/O-C.

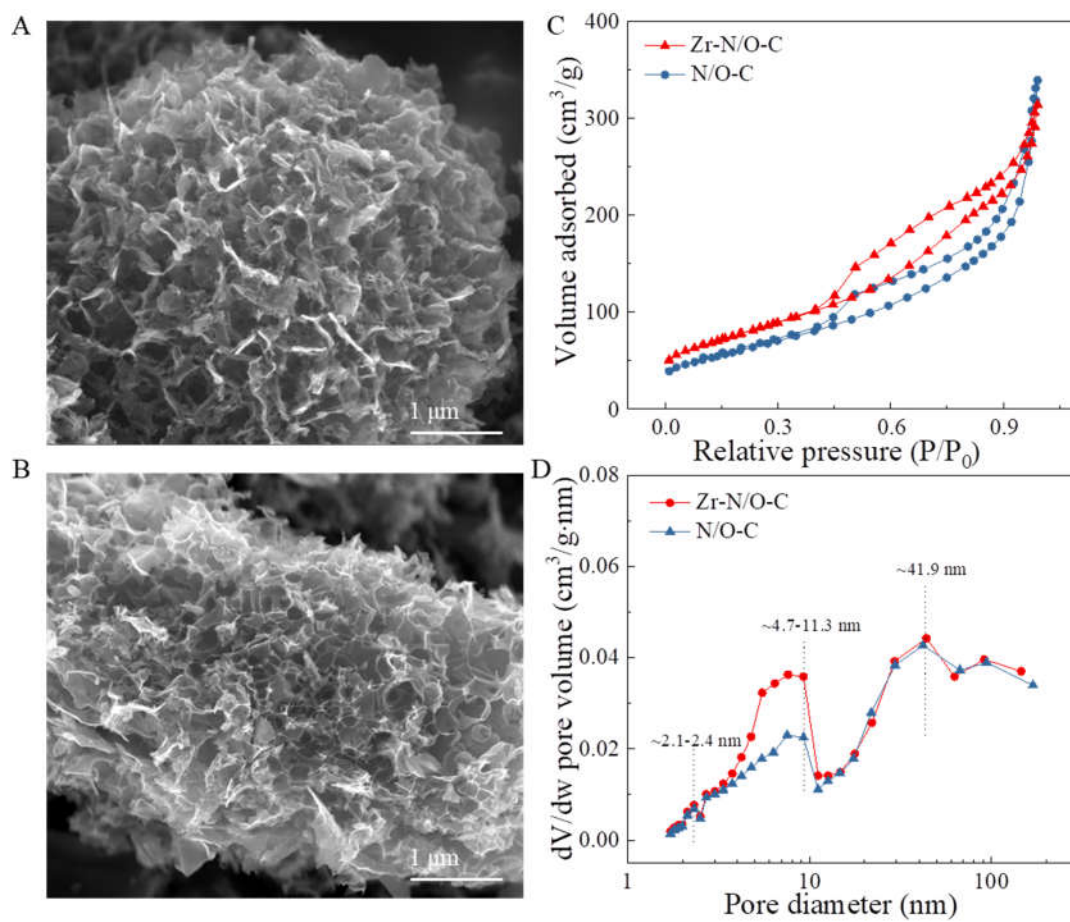


Figure S5 Effect of Zr doping on microstructure. The overall SEM morphologies of the different catalysts. **(A)** Zr-N/O-C and **(B)** N/O-C. N_2 adsorption/desorption plots **(C)** and pore distribution **(D)** of the Zr-N/O-C and N/O-C.

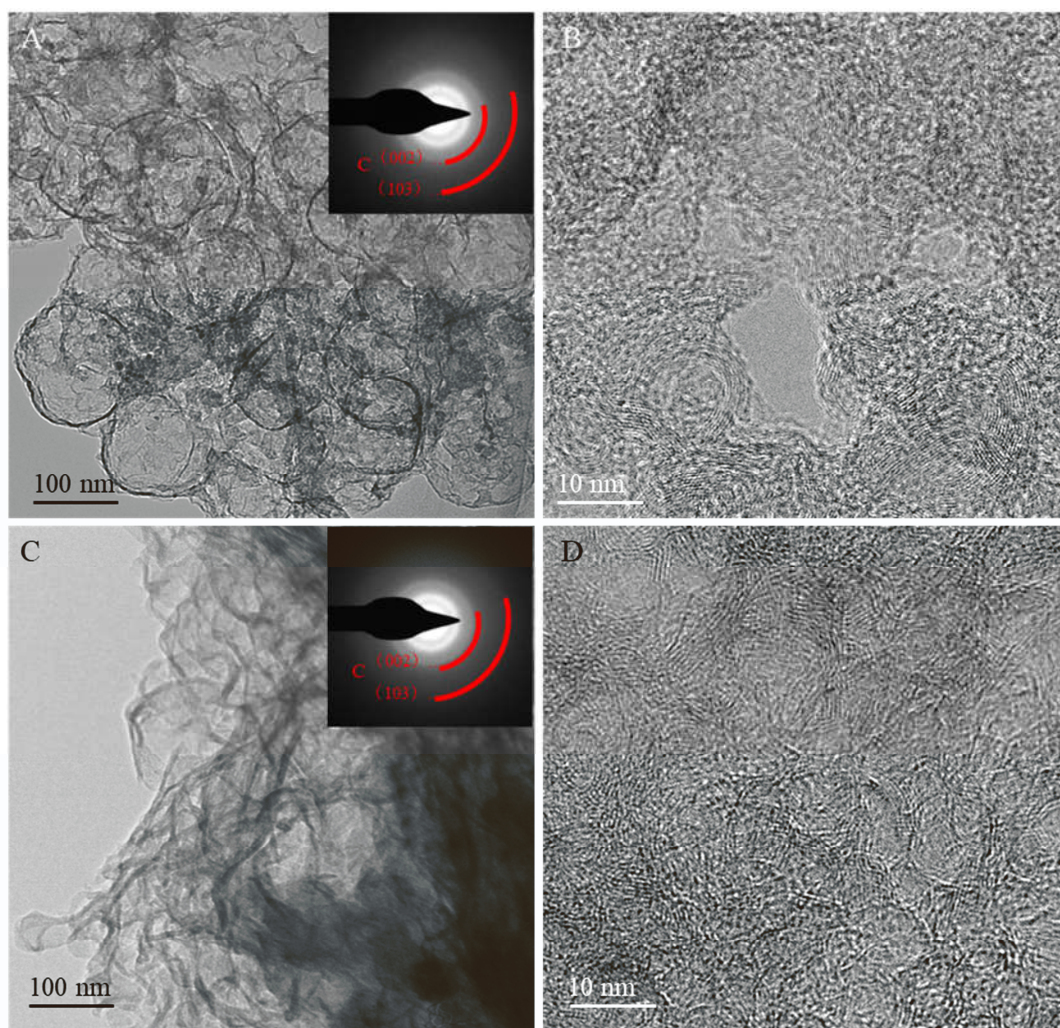


Figure S6 The TEM and HRTEM image of the different catalysts. **(A-B)**, TEM and HRTEM image of the Zr-N/O-C. No metal nanoparticles or oxide was observed. The inset is the selected area electron diffraction (SAED) pattern of the Zr-N/O-C. **(C-D)**, TEM and HRTEM image of the N/O-C. It is confirmed that the pristine N/O-C is the porous graphene of ~ 5 layers. The inset is the SAED pattern of the N/O-C.

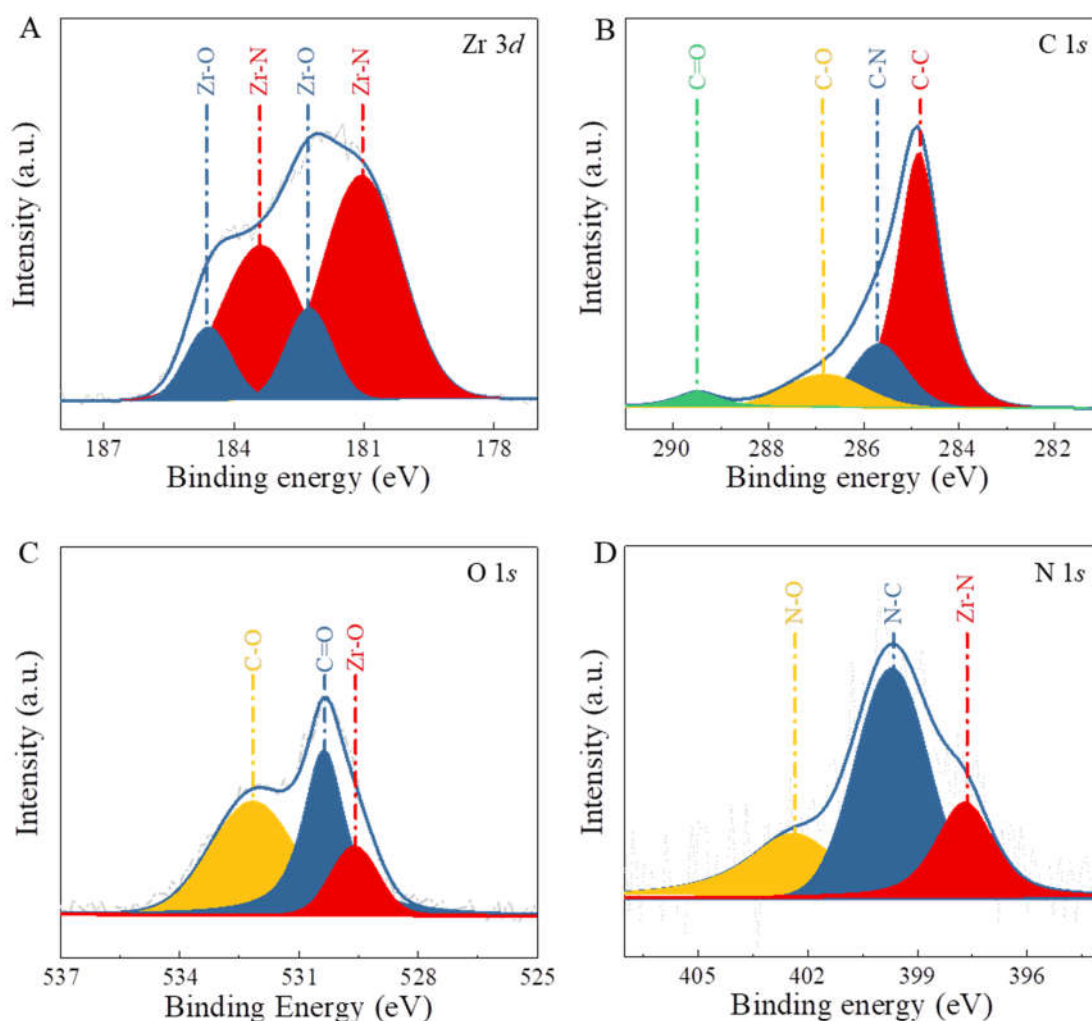


Figure S7 The XPS spectra for Zr 3d (A), C 1s (B), O 1s (C) and N 1s (D) of the Zr-N/O-C. The C 1s XPS spectra manifests four peaks at binding energies of 284.8, 285.7, 286.8 and 289.4 eV, which are assigned to graphitic sp^2 carbon (C-C), carbon coordinated with doped N (C-N), carbon coordinated with doped O (C-O) and sp^2 carbon (C=O) bonds, respectively¹. The O 1s spectra manifests three peaks at binding energies of 529.6, 530.8, 286.8 and 532.4 eV, which are assigned to Zr-O, C=O and C-O, respectively. The doping of O changes the charge density of C matrix, which is beneficial to ORR².

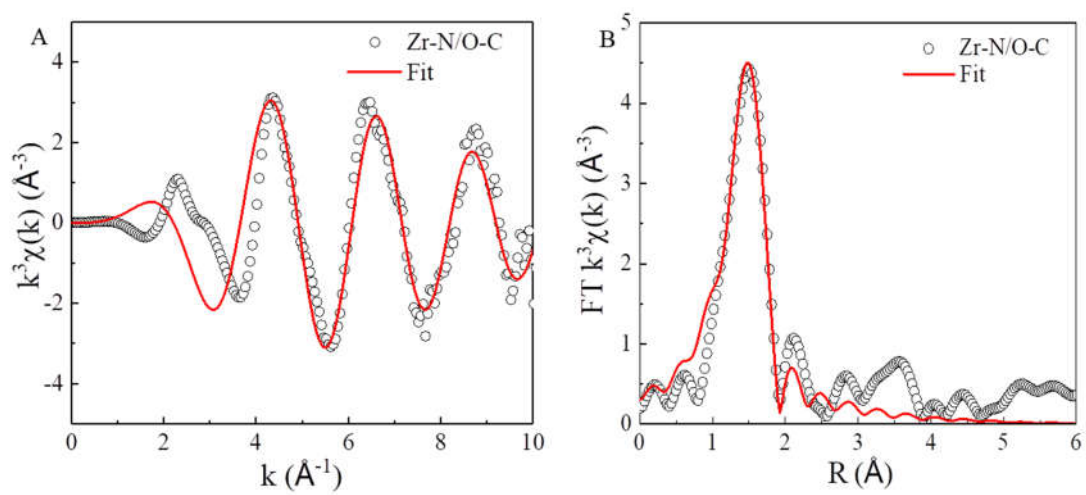


Figure S8 (A) The corresponding EXAFS k-space fitting results of the Zr-N/O-C. (B) FT-EXAFS fitting curves of the Zr-N/O-C. The best-fit structural parameters are listed in Supplementary Table 3.

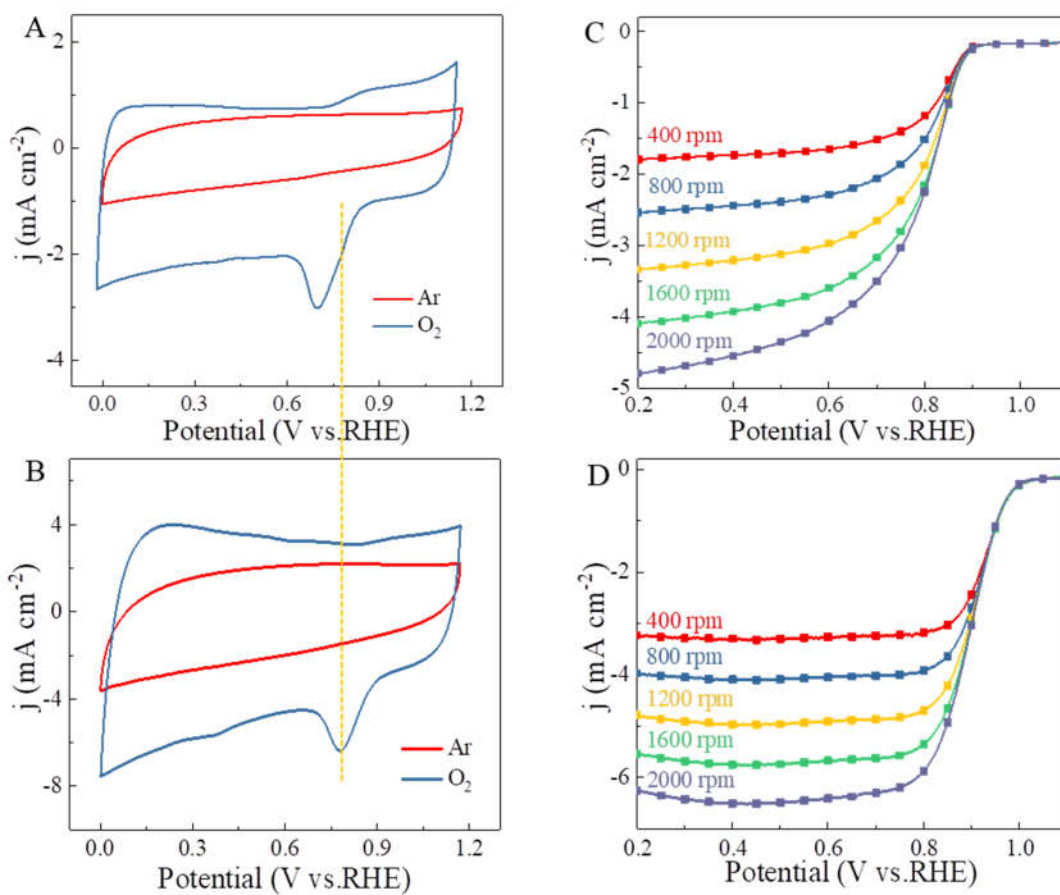


Figure S9 (A-B) CV curves of the N/O-C and Zr-N/O-C in 0.1 M KOH solution within a potential range from 0 to 1.2 V (Scan rate: 50 mV s⁻¹), respectively. **(C-D)** LSV curves of the N/O-C and Zr-N/O-C catalysts with different rotation rates during the RDE test.

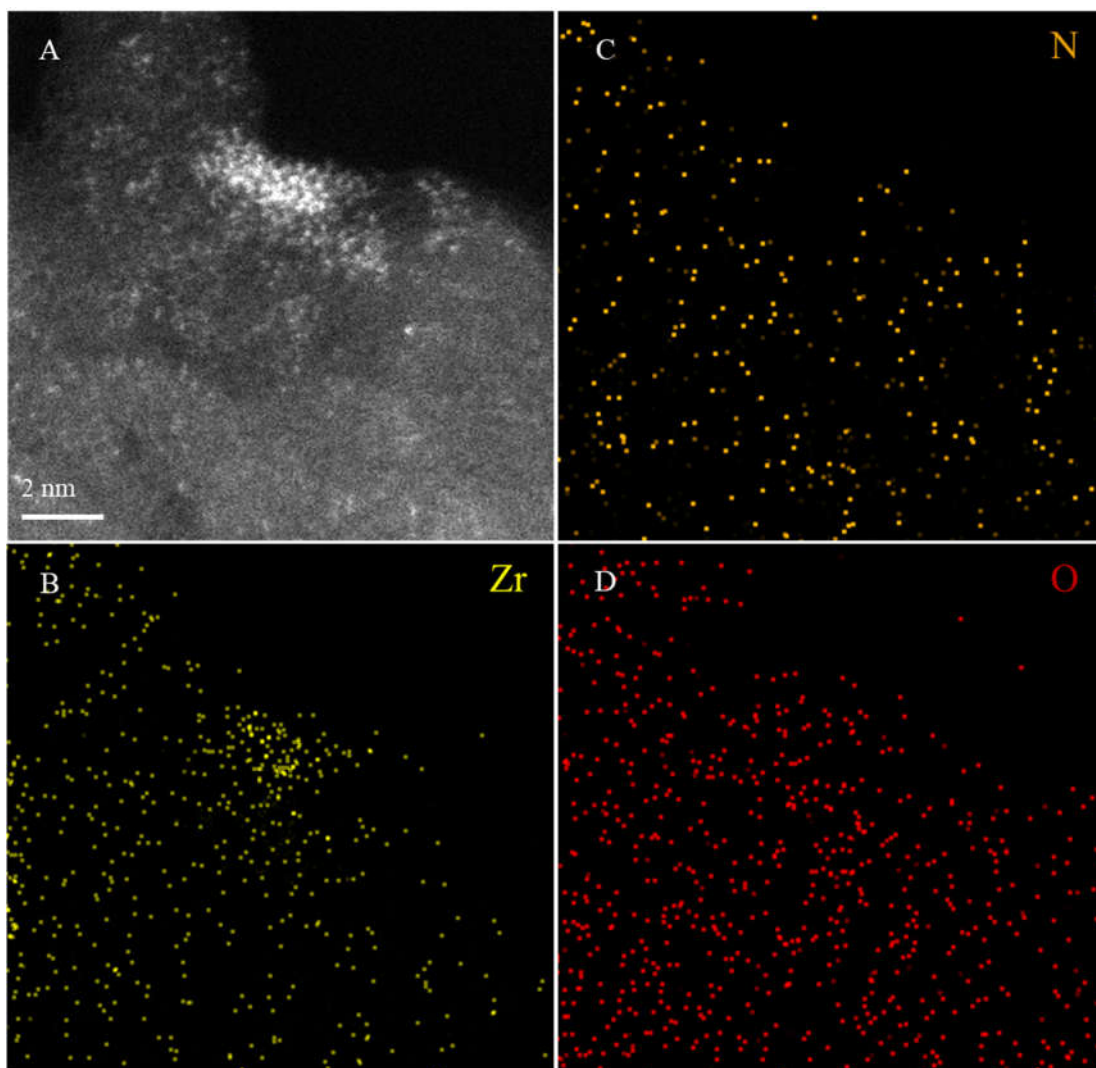


Figure S10 Morphology changes of Zr-N/O-C after 10000 continuous potential cycle. The atomic Zr dots are segregated to form some Zr clusters after a long-term cycling.

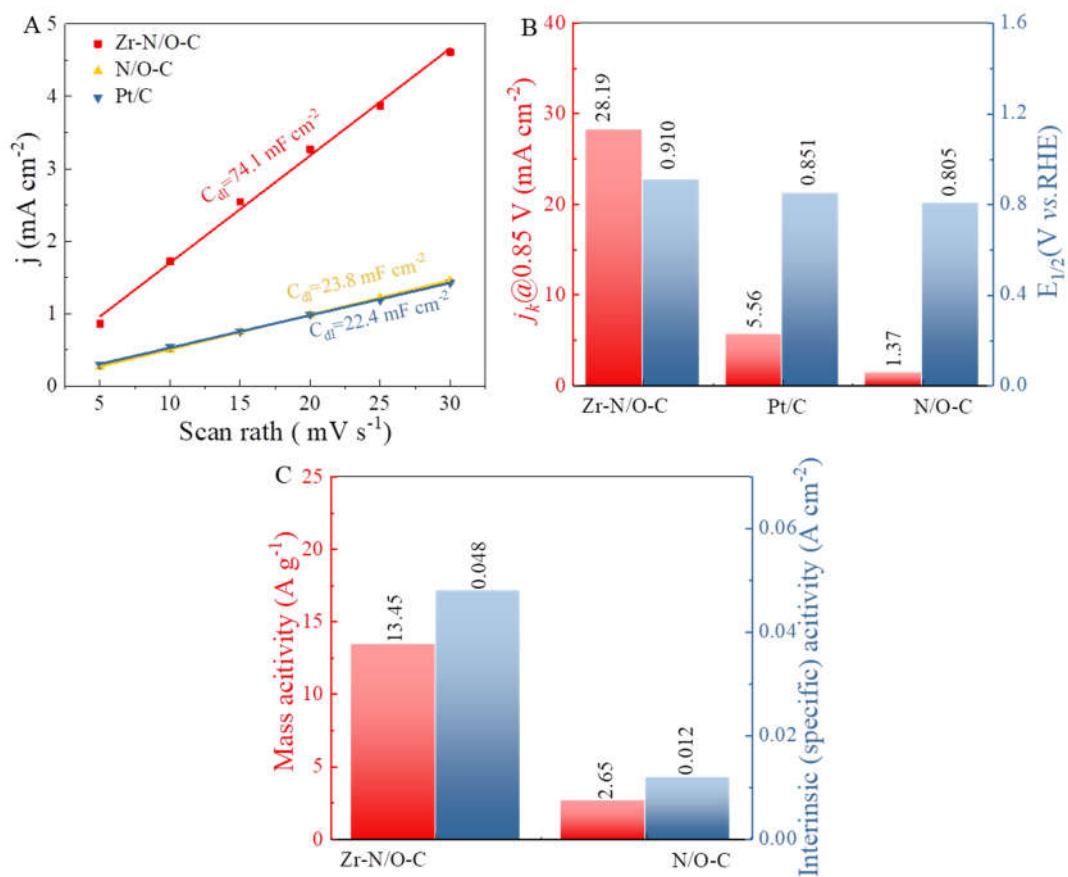


Figure S11 The different performance of catalysts. **(A)** C_{dl} , **(B)** Comparison of $E_{1/2}$ and j_k (0.85 V vs. RHE)³, **(C)** Mass activity and Interinsic activity.

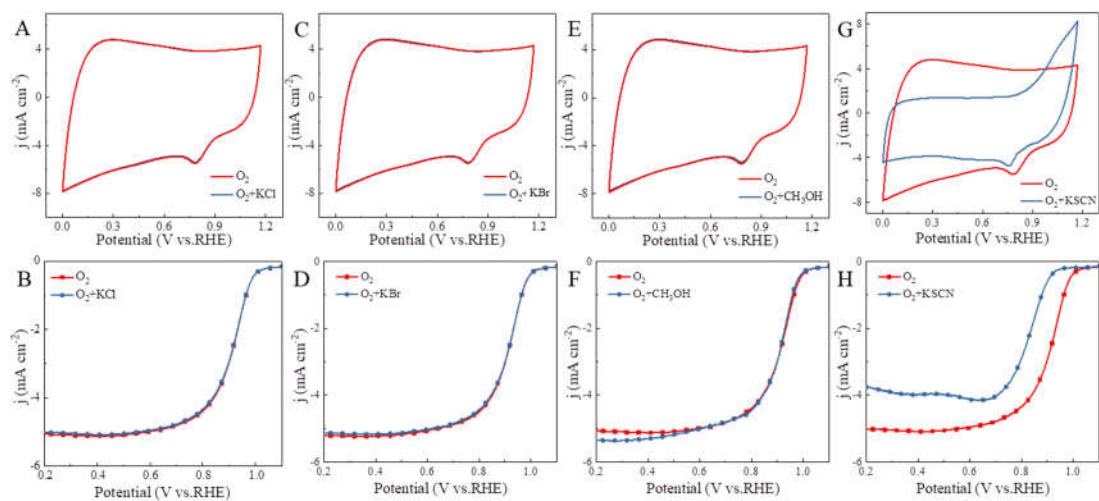


Figure S12 CV and LSV measurements were carried out by adding different anions (0.01 M) into the solution. **(A,B)** KCl. **(C,D)** KBr. **(E,F)** CH₃OH. **(G,H)** KSCN.

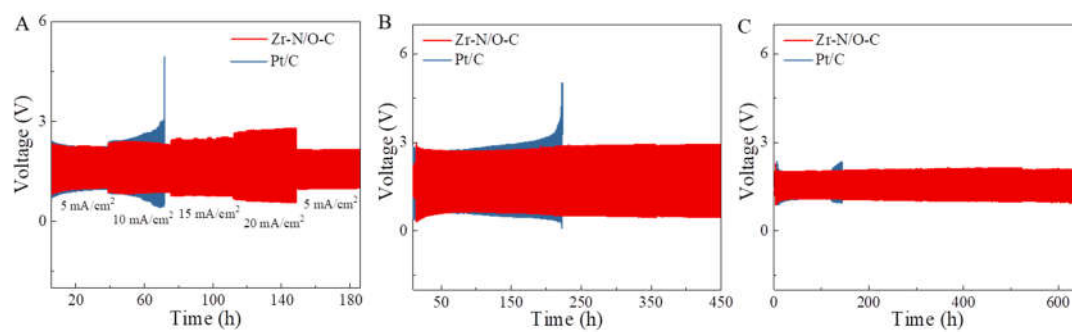


Figure S13 (A) Charge-discharge curves at different current densities. (B) and (C) The charge-discharge cycle performances of Zn-air batteries at -10 and 50 °C, respectively.

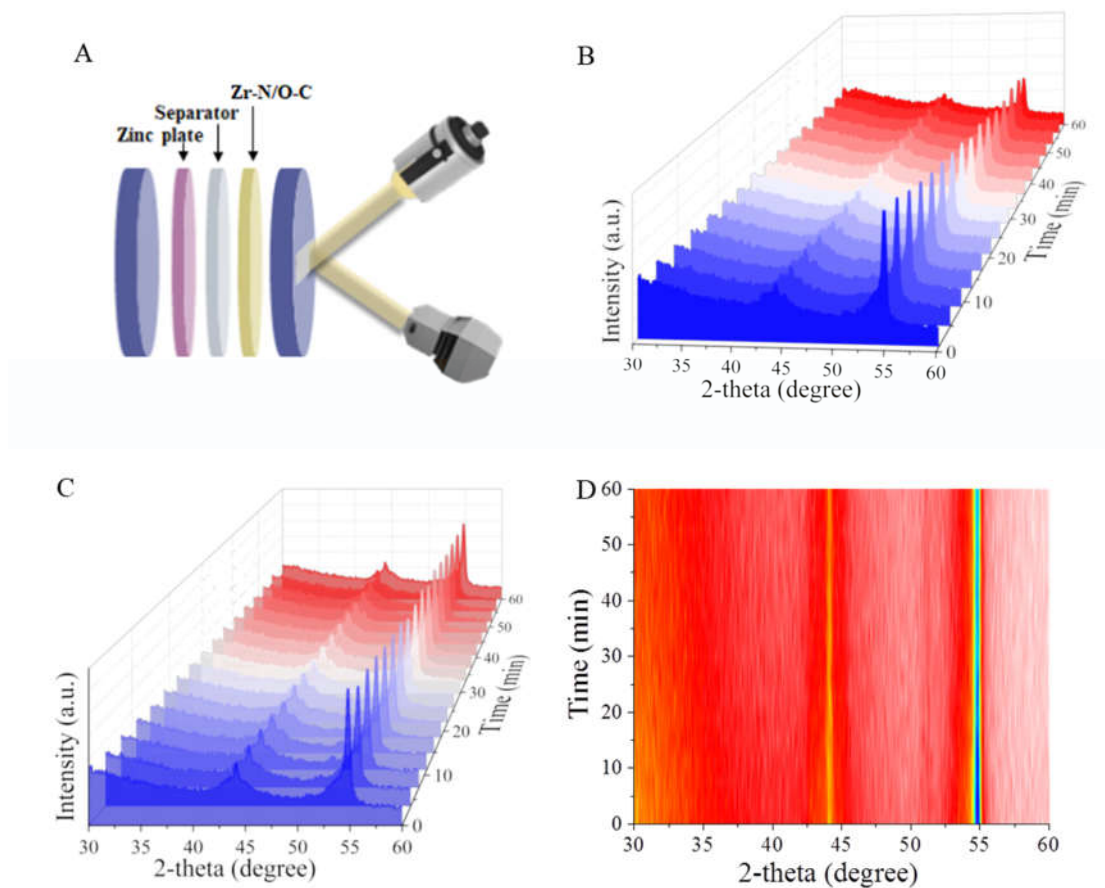


Figure S14 (A) Schematic diagram of in-situ experiments. In-situ XRD patterns of Zn-air batteries during discharging: (B) Zr-N/O-C electrode and (C) N/O-C electrode. (D) In-situ XRD contour plots of Zn-air batteries with pure carbon electrodes during discharging.

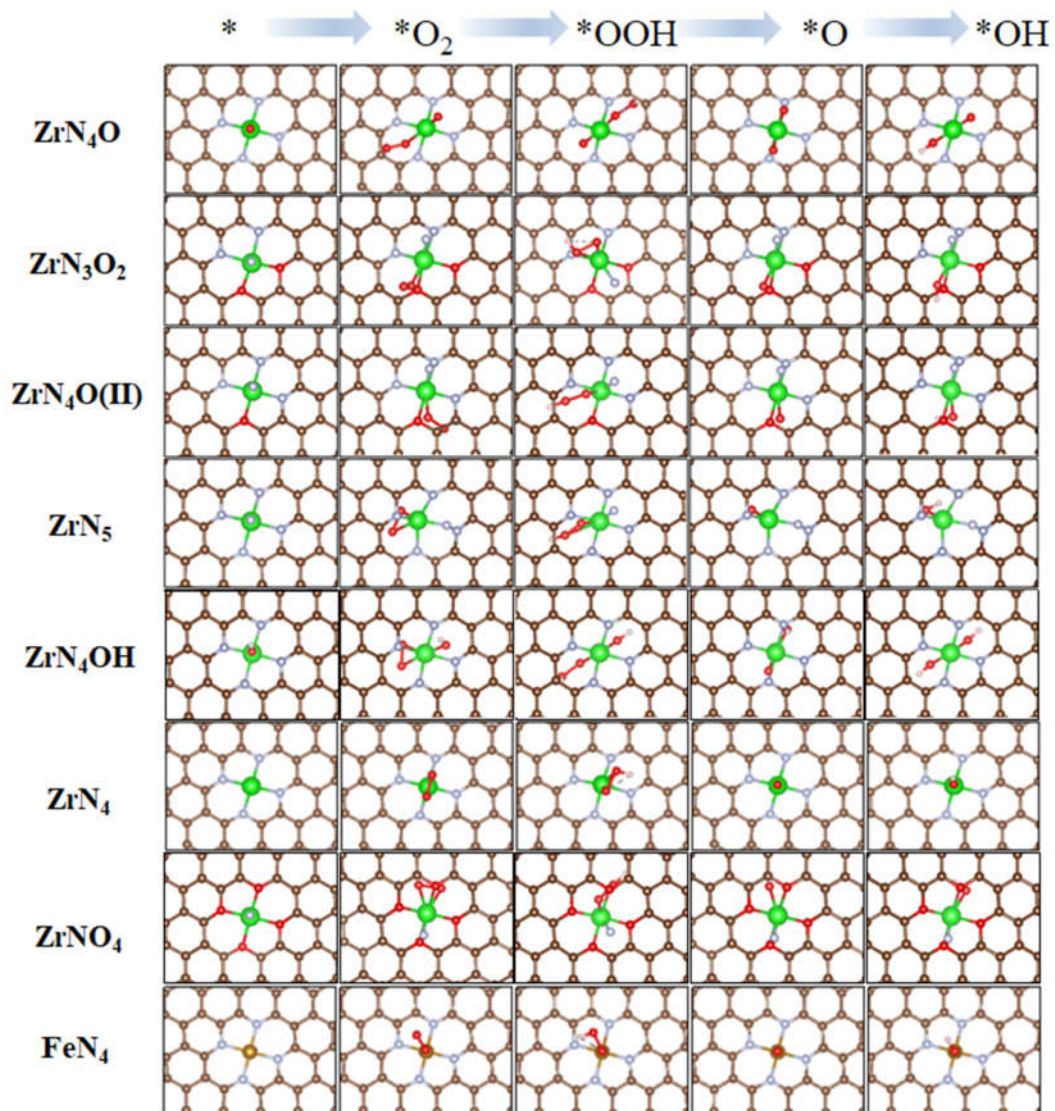


Figure S15 Proposed configurations for the reaction centers and the key reaction intermediates.

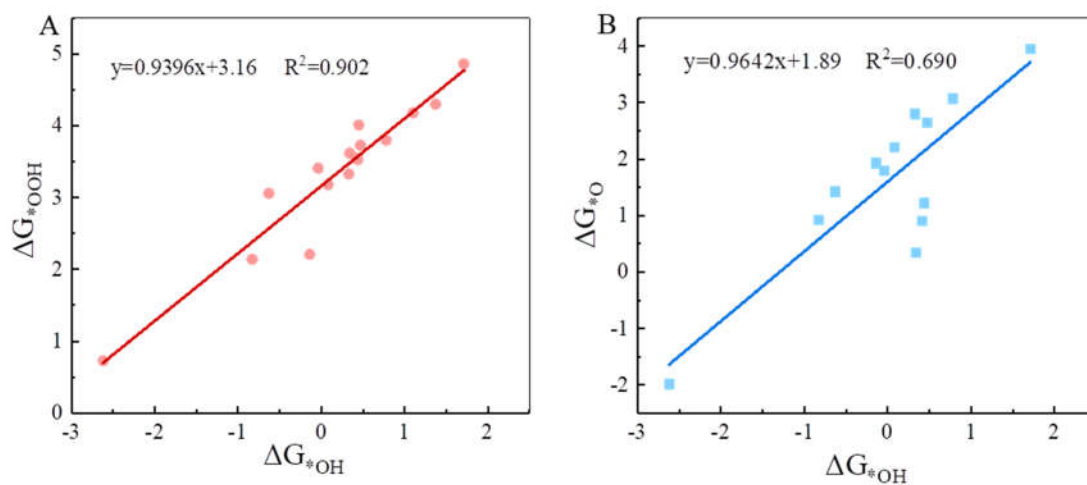


Figure S16 Linear relationship profiles of (A) ΔG_{*OOH} and (B) ΔG_{*O} as a function of ΔG_{*OH} .

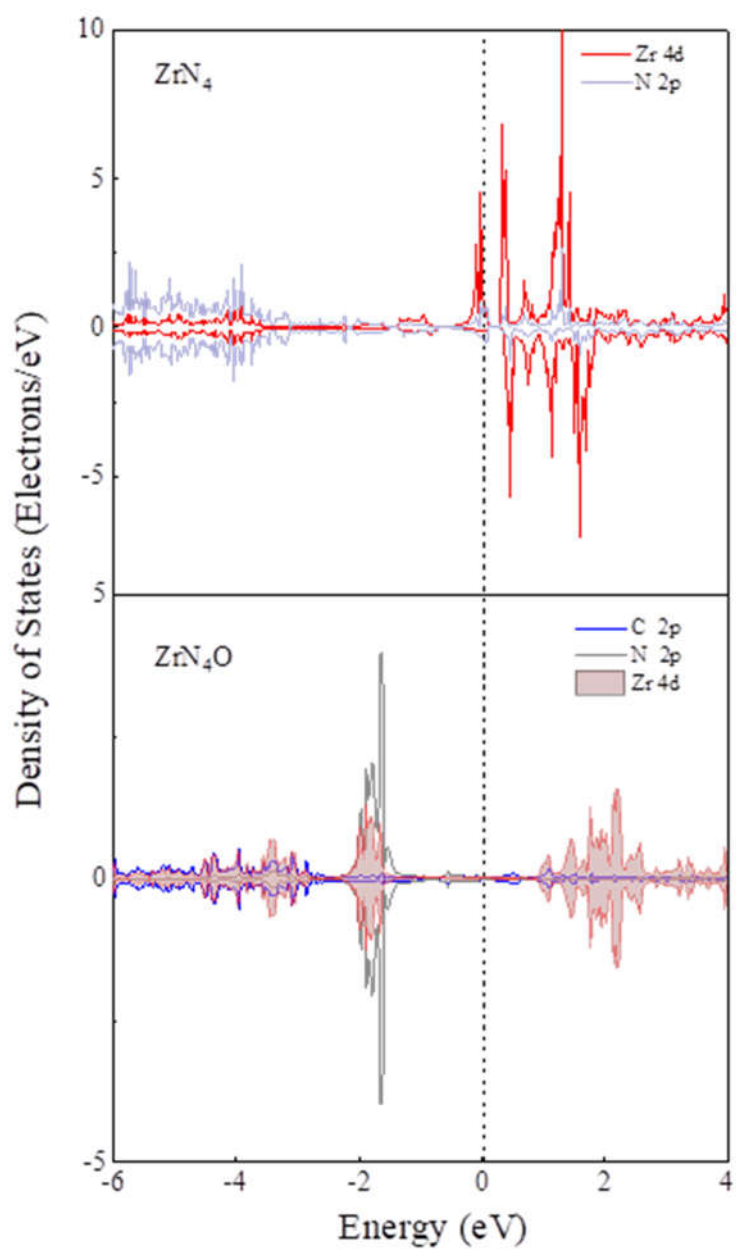


Figure S17 Partial density of states for ZrN_4 and ZrN_4O moieties, respectively.

Table S1 Metal concentration in the different samples determined by ICP-AES.

Samples	Metal concentration (wt.%)
Zr-N/O-C	2.93 (Zr)

Table S2 Elemental quantification (wt.%) determined by XPS and TEM elemental mapping for the Zr-N/O-C.

Samples	C	N	O	Zr
Zr-N/O-C (XPS)	78.30	6.96	11.85	2.89
Zr-N/O-C (TEM)	82.00	4.98	10.24	2.78

Table S3 EXAFS fitting parameters at the Zr K-edge for various samples ($S_0^2=0.94$)

Sample	Shell	N^a	$R(\text{\AA})^b$	$\sigma^2 \times 10^3 (\text{\AA}^2)^c$	$\Delta E_0 (\text{eV})^d$	R factor
Zr foil	Zr-Zr	12	3.21 ± 0.01	9.8 ± 0.4	-5.0 ± 0.6	0.003
ZrO ₂	Zr-O	8.7 ± 2.4	2.11 ± 0.02	12.6 ± 2.5	-8.7 ± 2.4	0.017
	Zr-Zr	4.7 ± 1.0	3.45 ± 0.01	6.5 ± 1.0	-9.5 ± 2.2	
Zr-N/O-C	Zr-N/O	5.2 ± 0.9	2.01 ± 0.01	7.8 ± 1.3	-10.4 ± 1.6	0.018

Table S4 Comparison of ORR performance between the Zr-N/O-C and other non-precious catalysts reported in the literatures under O₂-saturated 0.1 M KOH solution.

	Electrocatalysts	E _(onset) (V vs.RHE)	E _(1/2) (V vs.RHE)	Ref.
1	Zr-N/O-C	1.000	0.910	This work
4	CAN-Pc(Fe/Co)	0.940	0.840	4
5	Cu-N/O-C-ICHP	0.970	0.850	5
6	Mn/C-NO	0.940	0.860	6
7	Zn-N/O-C-1	0.960	0.875	7
8	Co-N/S DSHCN-3.5	0.989	0.880	8
9	WN ₅	1.010	0.880	9
10	Fe/N/S-CNTs	0.987	0.887	10
11	Fe-0.5-950	0.970	0.890	11
12	Sc@NC-750	0.990	0.890	12
13	Cu-SAs/N/O-C	1.000	0.895	13
14	Fe-ISAs/CN	0.986	0.900	14
15	Fe _{SA} -N/O-C	0.960	0.900	15
16	Fe SAs-N/C-20	0.970	0.909	16

SUPPLEMENTAL REFERENCES

1. Jia, Y., Zhang, L., Zhuang, L., Liu, H., Yan, X., Wang, X., Liu, J., Wang, J., Zheng, Y., and Xiao, Z. (2019). Identification of active sites for acidic oxygen reduction on carbon catalysts with and without nitrogen doping. *Nat. Catal.* **2**, 688-695.
2. Ferrari, A.C., and Basko, D.M. (2013). Raman spectroscopy as a versatile tool for studying the properties of graphene. *Nat. Nanotechnol.* **8**, 235-246.
3. Wu, G., More, K.L., Johnston, C.M., and Zelenay, P. (2011). High-performance electrocatalysts for oxygen reduction derived from polyaniline, iron, and cobalt. *Science* **332**, 443-447.
4. Yang, S., Yu, Y., Dou, M., Zhang, Z., Dai, L., and Wang, F. (2019). Two-dimensional conjugated aromatic networks as high-site-density and single-atom electrocatalysts for the oxygen reduction reaction. *Angew. Chem. Int. Ed.* **58**, 14724-14730.
5. Wang, T., Yang, R., Shi, N., Yang, J., Yan, H., Wang, J., Ding, Z., Huang, W., Luo, Q., and Lin, Y. (2019). Cu, N-codoped carbon nanodisks with biomimic stomata-like interconnected hierarchical porous topology as efficient electrocatalyst for oxygen reduction reaction. *Small* **15**, 1902410.
6. Yan, H., Xie, Y., Jiao, Y., Wu, A., Tian, C., Zhang, X., Wang, L., and Fu, H. (2018). Holey reduced graphene oxide coupled with an Mo₂N-Mo₂C heterojunction for efficient hydrogen evolution. *Adv. Mater.* **30**, 1704156.
7. Li, J., Chen, S., Yang, N., Deng, M., Ibraheem, S., Deng, J., Li, J., Li, L., and Wei, Z. (2019). Ultrahigh-loading zinc single-atom catalyst for highly efficient oxygen reduction in both acidic and alkaline media. *Angew. Chem. Int. Ed.* **58**, 7035-7039.
8. Wang, T., Yang, C., Liu, Y., Yang, M., Li, X., He, Y., Li, H., Chen, H., and Lin, Z. (2020). Dual-shelled multidoped hollow carbon nanocages with hierarchical porosity for high-performance oxygen reduction reaction in both alkaline and acidic media. *Nano Lett.* **20**, 5639-5645.
9. Chen, Z., Gong, W., Liu, Z., Cong, S., Zheng, Z., Wang, Z., Zhang, W., Ma, J., Yu, H., and Li, G. (2019). Coordination-controlled single-atom tungsten as a non-3d-metal oxygen reduction reaction electrocatalyst with ultrahigh mass activity. *Nano Energy* **60**, 394-403.
10. Jin, H., Zhou, H., Li, W., Wang, Z., Yang, J., Xiong, Y., He, D., Chen, L., and Mu, S. (2018). In situ derived Fe/N/S-codoped carbon nanotubes from ZIF-8 crystals as efficient electrocatalysts for the oxygen reduction reaction and zinc-air batteries. *J. Mater. Chem. A* **6**, 20093-20099.
11. Zitolo, A., Goellner, V., Armel, V., Sougrati, M.-T., Mineva, T., Stievano, L., Fonda, E., and Jaouen, F. (2015). Identification of catalytic sites for oxygen reduction in iron-and nitrogen-doped graphene materials. *Nat. Mater.* **14**, 937-942.
12. Wen, X., Duan, Z., Bai, L., and Guan, J. (2019). Atomic scandium and

- nitrogen-codoped graphene for oxygen reduction reaction. *J. Power Sources* **431**, 265-273.
13. Qu, Y., Li, Z., Chen, W., Lin, Y., Yuan, T., Yang, Z., Zhao, C., Wang, J., Zhao, C., and Wang, X. (2018). Direct transformation of bulk copper into copper single sites via emitting and trapping of atoms. *Nat. Catal.* **1**, 781-786.
 14. Chen, Y., Ji, S., Wang, Y., Dong, J., Chen, W., Li, Z., Shen, R., Zheng, L., Zhuang, Z., Wang, D., and Li, Y. (2017). Isolated single iron atoms anchored on N-doped porous carbon as an efficient electrocatalyst for the oxygen reduction reaction. *Angew. Chem. Int. Ed.* **56**, 6937-6941.
 15. Jiao, L., Zhang, R., Wan, G., Yang, W., Wan, X., Zhou, H., Shui, J., Yu, S.H., and Jiang, H.L. (2020). Nanocasting SiO₂ into metal-organic frameworks imparts dual protection to high-loading Fe single-atom electrocatalysts. *Nat. Commun.* **11**, 2831.
 16. Jiang, R., Li, L., Sheng, T., Hu, G., Chen, Y., and Wang, L. (2018). Edge-site engineering of atomically dispersed Fe-N₄ by selective C-N bond cleavage for enhanced oxygen reduction reaction activities. *J. Am. Chem. Soc.* **140**, 11594-11598.